



# Three-dimensionally ordered macroporous Au/CeO<sub>2</sub>-Co<sub>3</sub>O<sub>4</sub> catalysts with nanoporous walls for enhanced catalytic oxidation of formaldehyde

Baocang Liu<sup>a,b</sup>, Yang Liu<sup>a</sup>, Changyan Li<sup>a,b</sup>, Wenting Hu<sup>a</sup>, Peng Jing<sup>a</sup>, Qin Wang<sup>a</sup>, Jun Zhang<sup>a,b,\*</sup>

<sup>a</sup> College of Chemistry and Chemical Engineering, Inner Mongolia University, Hohhot 010021, PR China

<sup>b</sup> College of Life Science, Inner Mongolia University, Hohhot 010021, PR China

## ARTICLE INFO

### Article history:

Received 6 April 2012

Received in revised form 3 August 2012

Accepted 9 August 2012

Available online 16 August 2012

### Keywords:

Three-dimensionally ordered macroporous

Au/CeO<sub>2</sub>-Co<sub>3</sub>O<sub>4</sub> catalysts

HCHO catalytic oxidation

Synergistic effect

Catalytic mechanism

## ABSTRACT

Three-dimensionally ordered macroporous (3DOM) Au/CeO<sub>2</sub>-Co<sub>3</sub>O<sub>4</sub> catalysts were created via a precursor thermal decomposition-assisted colloidal crystal templating method. The 3DOM Au/CeO<sub>2</sub>-Co<sub>3</sub>O<sub>4</sub> catalysts possessed well-defined 3DOM structures with adjustable pore sizes, and their compositions, phase structures, and surface elemental valence states can be well controlled by solely adjusting the Ce/Co molar ratio. Moreover, the nanoporous walls with pore sizes around ~3–4 nm were created in 3DOM Au/CeO<sub>2</sub>-Co<sub>3</sub>O<sub>4</sub> catalysts through the thermal decomposition of Co and Ce oxalate precursors during the preparation. The 3DOM Au/CeO<sub>2</sub>-Co<sub>3</sub>O<sub>4</sub> catalysts exhibited superior catalytic activity for formaldehyde (HCHO) catalytic oxidation into CO<sub>2</sub> and H<sub>2</sub>O with a 100% conversion rate at temperatures as low as ~39 °C. A catalytic mechanism of the synergistic effect between CeO<sub>2</sub> and Co<sub>3</sub>O<sub>4</sub> supports, which greatly accelerates the surface active oxygen migration and activates the Au species, was proposed for explaining the enhanced HCHO catalytic oxidation over 3DOM Au/CeO<sub>2</sub>-Co<sub>3</sub>O<sub>4</sub> catalysts. The well-controlled method for creation of 3DOM Au/CeO<sub>2</sub>-Co<sub>3</sub>O<sub>4</sub> catalysts with nanoporous walls could be adopted for generation of other catalytic materials with mixed macroporous and mesoporous structures. The superior catalytic activity of 3DOM Au/CeO<sub>2</sub>-Co<sub>3</sub>O<sub>4</sub> catalysts makes them potentially applicable to indoor HCHO decontamination and industrial catalysis.

© 2012 Elsevier B.V. All rights reserved.

## 1. Introduction

Porous structured materials have attracted much research attention in recent years [1–3]. As a class of important porous structured materials, three-dimensionally ordered macroporous (3DOM) materials have particularly sparked great research interest and become a hotspot in the field of porous materials owing to their unique features of relatively high-specific surface area, large pore volume, periodical pore structure, tunable pore size, well-controlled surface characteristic, ordered channel network, and good penetrability [3,4]. Hence, 3DOM materials show great potential in applications such as photonic crystals [5], electrode materials [6,7], adsorption/desorption [8], and carrier/catalysts [4].

On account of their relatively high catalytic activity, oxide-supported noble metallic catalysts have been widely studied in application of heterogeneous catalysis including formaldehyde (HCHO) catalytic oxidation [9–24], monoxide (CO) oxidation [25,26], alcohol aerobic oxidation [27–29], and organic coupling

reaction [30,31]. A variety of oxide-supported noble metallic catalysts, such as Au/CeO<sub>2</sub> [9,11,12], Au/Co<sub>3</sub>O<sub>4</sub>-CeO<sub>2</sub> [13], Ag/MnO<sub>x</sub>-CeO<sub>2</sub> [14], Pt/MnO<sub>x</sub>-CeO<sub>2</sub> [15], Pd/TiO<sub>2</sub> [16], Pd/Beta [17], Pt/TiO<sub>2</sub> [18–20], Au/Fe<sub>2</sub>O<sub>3</sub> [10,20], Au/ZrO<sub>2</sub> [22,23], and Pd-Mn/Al<sub>2</sub>O<sub>3</sub> [24] catalysts, have been reported for HCHO catalytic oxidation. Shen et al. has found that powder Au/CeO<sub>2</sub> catalysts show superior catalytic activity for HCHO catalytic oxidation with a 100% catalytic conversion of HCHO into CO<sub>2</sub> and at moderate temperature of ~105 °C [11]. However, the temperature of HCHO catalytic oxidation with such catalysts still needs to be further lowered in order to meet the requirements for practical application. Zhang et al. created novel three-dimensionally ordered macroporous (3DOM) Au/CeO<sub>2</sub> catalysts with controlled pore sizes via a colloidal crystal template method. The complete conversion of HCHO into CO<sub>2</sub> and H<sub>2</sub>O via catalytic oxidation process over such Au/CeO<sub>2</sub> catalysts can be realized at ~75 °C, a much lower temperature than previously reported powder Au/CeO<sub>2</sub> catalysts [9]. This suggests that the oxide-supported noble metallic catalysts with novel 3DOM structures and architectures may result in the improvement of their catalytic functionality. In addition to the modulation of catalyst structures and architectures, the changes of noble metal species and support types can also result in the improvement of the catalytic activity of oxide-supported noble metallic catalysts. Álvarez-Galván et al. synthesized the

\* Corresponding author at: College of Chemistry and Chemical Engineering, Inner Mongolia University, No. 235, West University Road, Hohhot 010021, PR China. Tel.: +86 471 4992175; fax: +86 471 4992278.

E-mail address: [cejzhang@imu.edu.cn](mailto:cejzhang@imu.edu.cn) (J. Zhang).

Pd-MnO<sub>x</sub>/Al<sub>2</sub>O<sub>3</sub> catalysts, which show superior catalytic activity for complete HCHO catalytic oxidation at moderate temperatures around 80 °C [24]. Shen and co-workers developed Ag/MnO<sub>x</sub>-CeO<sub>2</sub> and Pt/MnO<sub>x</sub>-CeO<sub>2</sub> catalysts, with which HCHO can be completely oxidized at 100 °C and ambient temperature, respectively [14,15]. Ma et al. reported the catalytic performance of HCHO catalytic oxidation over mesoporous Au/Co<sub>3</sub>O<sub>4</sub>-CeO<sub>2</sub> catalysts, and the conversion of HCHO catalytic oxidation over such catalysts at room temperature is around 50% [13]. Thus, the oxide-supported noble metallic catalysts are believed to be one kind of effective catalysts for HCHO catalytic oxidation at relatively low temperature.

Among the most effective oxide-supported noble metallic catalysts, oxide-supported Au catalysts exhibit extraordinarily high activity in many reactions including HCHO catalytic oxidation due to their high catalytic efficiency. Under the catalysis of oxide-supported Au catalysts, HCHO could be catalytically converted into CO<sub>2</sub> and H<sub>2</sub>O via the catalytic oxidation process at relatively low temperature. However, most previously reported oxide-supported Au catalysts are in the form of nanopowders, and aggregation of Au nanoparticles on powder catalyst supports may occur during preparation, which greatly affects their catalytic activity. Therefore, the implementation of 3DOM structures into oxide-supported Au catalysts may result in novel catalysts with excellent catalytic functionality.

It is generally accepted that the catalytic activity of oxide-supported noble metallic catalysts is tightly correlated to their compositions, phase structures, surface elemental valence states as well as support types. Thus, the incorporation of other transition metallic oxides into the CeO<sub>2</sub> support may improve the catalytic activity of the Au/CeO<sub>2</sub> catalysts due to a synergistic effect between different oxide supports, which could greatly activate Au species, accelerate the migration rate of active oxygen on catalyst surface, and eventually enhance the catalytic activity.[13–15]

In this paper, we present a novel approach for creating 3DOM Au/CeO<sub>2</sub>-Co<sub>3</sub>O<sub>4</sub> catalysts with nanoporous walls. The three-dimensionally ordered geometry of Au/Co<sub>3</sub>O<sub>4</sub>-CeO<sub>2</sub> catalysts may have better permeability and diffusivity, and could afford unique macroporous and mesoporous structure for large amount of key catalyst species loading with less aggregation and good distribution in comparison to 2DAu/CeO<sub>2</sub>-Co<sub>3</sub>O<sub>4</sub> catalysts.[13] which is beneficial for improving catalytic performance. The obtained 3DOM Au/CeO<sub>2</sub>-Co<sub>3</sub>O<sub>4</sub> catalysts exhibited superior catalytic activity for HCHO catalytic oxidation into CO<sub>2</sub> and H<sub>2</sub>O with 100% conversion rate at the relatively low temperature of ~39 °C, which is, to the best of our knowledge, the lowest temperature of HCHO catalytic oxidation over oxide-supported Au catalysts ever reported.

## 2. Experimental

### 2.1. Catalyst preparation

#### 2.1.1. Synthesis of monodispersed PS colloidal spheres

Monodispersed polystyrene (PS) spheres were synthesized by a soap-free-emulsion polymerization method and were packed into colloidal crystal templates by centrifugation according to the previous report [9]. The detailed reaction conditions for synthesis of monodispersed PS colloidal spheres in various batches with average diameters of 200, 400, and 600 nm are shown in Table S1. The typical procedures for the preparation are as follows. Before preparation, styrene (St) monomer was washed with NaOH solution (0.1 M) and distilled water four times in a separatory funnel. Then, a certain amount of pre-treated St monomer and distilled water were added to a 1000 mL three neck round-bottomed flask equipped with a condenser, a thermometer, and a pipe for nitrogen introduction. The mixture was magnetically stirred, and nitrogen

was introduced to remove the air inside the flask and afford an inert reaction atmosphere. Next, following the addition of K<sub>2</sub>S<sub>2</sub>O<sub>8</sub> solution to initiate polymerization, the temperature of the reaction system was raised to 70 °C, and the polymerization reaction was conducted under this temperature for 28 h. After the reaction was finished, the reaction system was naturally cooled to room temperature, and filtered to obtain the homogenous latex with nearly monodispersed PS colloidal spheres.

#### 2.1.2. Assembly of 3DOM PS colloidal crystal templates

The 3DOM PS colloidal crystal templates were assembled via a centrifugation method [9]. A certain amount of PS latex was ultrasonicated to form a uniform emulsion and centrifuged at a rate of 4 krpm for 4 h. Depending on the sizes of PS colloidal spheres, the centrifuging time could be slightly variable. After the PS colloidal spheres were fully precipitated, the supernatant was carefully removed using a dropper. The centrifuge tube containing the well-arranged PS colloidal spheres was then dried at room temperature to obtain the final highly ordered PS colloidal crystal templates for synthesis of 3DOM CeO<sub>2</sub>-Co<sub>3</sub>O<sub>4</sub> supports.

#### 2.1.3. Synthesis of 3DOM CeO<sub>2</sub>-Co<sub>3</sub>O<sub>4</sub> supports

The 3DOM CeO<sub>2</sub>-Co<sub>3</sub>O<sub>4</sub> supports with different Ce/Co molar ratios were synthesized via a precursor thermal decomposition-assisted colloidal crystal templating method. Typically, appropriate amounts of Ce(NO<sub>3</sub>)<sub>3</sub>•6H<sub>2</sub>O and Co(Ac)<sub>2</sub>•4H<sub>2</sub>O precursors were dissolved in the mixed solvents of EtOH (10 mL) and CH<sub>3</sub>COOH (10 mL) to achieve the precursor solution. PS colloidal crystal templates (4 g) were carefully introduced into a Buchner funnel, to which a vacuum was applied. Then, the precursor solution was added dropwise into the funnel until the PS colloidal crystal templates were completely permeated. The PS colloidal crystal templates permeated with Ce(NO<sub>3</sub>)<sub>3</sub> and Co(Ac)<sub>2</sub> precursor solution were then dried at 60 °C for 1.5 h. The dried composites were soaked in 20 mL of oxalic acid solution (6 g oxalic acid in 20 mL of ethanol) for 5–10 min, and then underwent an additional vacuum filtration and drying step. The above procedures were repeated four times to ensure the complete permeation of Ce(NO<sub>3</sub>)<sub>3</sub> and Co(Ac)<sub>2</sub> precursor solution into the interstices of PS colloidal crystal templates. The PS colloidal crystal templates were removed by annealing in the furnace at 300 °C for 5 h, following the calcination at 450 °C for 6 h with the heating rate controlled at 1 °C min<sup>-1</sup> to obtain 3DOM CeO<sub>2</sub>-Co<sub>3</sub>O<sub>4</sub> supports.

#### 2.1.4. Synthesis of 3DOM Au/CeO<sub>2</sub>-Co<sub>3</sub>O<sub>4</sub> catalysts

The synthesis of 3DOM Au/CeO<sub>2</sub>-Co<sub>3</sub>O<sub>4</sub> catalysts was carried out via a gas bubbling-assisted deposition precipitation method developed in our lab [9]. The typical procedures for the preparation were as follows: 3DOM CeO<sub>2</sub>-Co<sub>3</sub>O<sub>4</sub> supports (0.2 g) with different pore sizes were introduced into a HAuCl<sub>4</sub> solution. 4.2, 8.4, 12.6, and 16.8 mL HAuCl<sub>4</sub> solutions (1 g/L) diluted with 100 mL distilled water were used to prepare 3DOM Au/CeO<sub>2</sub>-Co<sub>3</sub>O<sub>4</sub> catalysts with nominal Au contents of 1, 2, 3, and 4 wt%, respectively. After bubbling the solution with air for 0.5 h, the pH value was adjusted to 9 by adding Na<sub>2</sub>CO<sub>3</sub> (0.2 mol/L) to precipitate Au ions. The reaction system was further vigorously bubbled with air for 2 h, and let stand for 24 h. Then, the product was filtered and washed until the Cl<sup>-</sup> was completely removed according to a test with AgNO<sub>3</sub>, and the final products were dried in an oven at 60 °C to obtain the desired 3DOM Au/CeO<sub>2</sub>-Co<sub>3</sub>O<sub>4</sub> catalysts with various pore sizes. For convenience, the obtained 3DOM Au/CeO<sub>2</sub>-Co<sub>3</sub>O<sub>4</sub> catalyst was nominated as 3DOM Au ~ *m* wt%/*n*CeO<sub>2</sub>-Co<sub>3</sub>O<sub>4</sub> in the following discussion, where *m* refers to the nominal Au loading content in weight percentage (wt%), and *n* is the Ce/Co molar ratio for the preparation of 3DOM Au/CeO<sub>2</sub>-Co<sub>3</sub>O<sub>4</sub> catalyst.

## 2.2. Characterization

Powder X-ray diffraction (XRD) was used to characterize the phase structures of the 3DOM Au/CeO<sub>2</sub>-Co<sub>3</sub>O<sub>4</sub> catalysts. Measurements were performed using a PuXi-XD3 diffractometer (China) operated at 36 kV and 20 mA with a slit of 1/2 at a scanning rate of 2° min<sup>-1</sup> in a scanning range of 2 $\theta$  = 10–80°, using CuK $\alpha$  radiation ( $\lambda$  = 0.15406 nm). Samples for XRD measurements were prepared by gently crushing the obtained products with a mortar and pestle and were placed in a quartz glass holder for characterization. Transmission electron microscopy (TEM) characterization was performed on a JEM-2010 system operated at an acceleration voltage of 120 kV to evaluate the structure, geometry, pore size, and Au distribution in 3DOM Au/CeO<sub>2</sub>-Co<sub>3</sub>O<sub>4</sub> catalysts. Samples for TEM analysis were prepared by drying a drop of PS latex or catalyst dispersion on an amorphous carbon coated copper grid for observation. Scanning electron micrographs were recorded with a Hitachi S-3400N scanning electron microscope (SEM) to determine the PS sizes, colloidal crystal arrangement, and catalyst pore sizes. Samples for SEM measurements were deposited on silicon substrates and coated with a 5 nm Pt for characterization. Surface area measurements were performed on an ASAP 2010 Brunauer–Emmett–Teller (BET) analyzer. X-ray photoelectron spectroscopy (XPS) measurements were carried out on a XSAM800 X-ray photoelectron spectrometer with an AlK $\alpha$  (1486.67 eV) excitation source to determine the existence and valence states of Au nanoparticles in 3DOM Au/CeO<sub>2</sub>-Co<sub>3</sub>O<sub>4</sub> catalysts. Actual Au content in the catalysts was estimated with a VARIAN VISTA-MPX ICP-Mass spectrometer (MS, USA), and actual Ce and Co contents in the catalysts were tested using a ICPS-8100 ICP-AES spectrometer (SHIMADZU, Japan).

## 2.3. Catalytic tests

The catalytic activity tests were carried out in a continuous flow fixed-bed reactor consisting of a U-shape quartz tube (inner diameter 0.6 cm) attached on a PX-200 catalyst characterization system (Tianjin Pengxiang Co., Ltd.). A gas chromatograph (GC-2014C, Shimadzu) was equipped on PX-200 catalyst characterization system for online analysis of the products. A TCD detector was applied to monitor the products online. 200 mg catalyst was loaded into the reactor. The feeding gas was 0.06 vol.% HCHO (8 ppm) balanced with the air generated by passing an air flow, which was previously passed through 5 A zeolites and solid NaOH to remove H<sub>2</sub>O and CO<sub>2</sub>, through a solution of 36 wt.% HCHO at 0 °C. The space velocity of the experiment was 1.5  $\times$  10<sup>4</sup> mL h<sup>-1</sup> g<sup>-1</sup>. The activity of the catalysts on HCHO oxidation was estimated by the conversion rate of CO<sub>2</sub> following a HCHO oxidation process. The concentration of CO<sub>2</sub> resulting from HCHO oxidation was measured with gas chromatograph (GC-2014C, Shimadzu) equipped on PX-200 catalyst characterization system to estimate the HCHO oxidation online. The detailed experiments were conducted following the procedures described as follows: First, the gas, which had been pre-cleaned to remove H<sub>2</sub>O and CO<sub>2</sub>, was continuously flowed through 3DOM Au/CeO<sub>2</sub>-Co<sub>3</sub>O<sub>4</sub> catalysts in the reactor. The reactor was then heated to 80 °C to remove the substances adsorbed on the surface of the catalysts and subsequently cooled to room temperature. Next, the feeding gas containing 0.06 vol.% HCHO was introduced into the reactor continuously. The reactor was heated to different temperatures under air flow (50 mL min<sup>-1</sup>) to evaluate the temperature-dependent catalytic activity of the catalysts. The absorbed HCHO will be catalytically converted into CO<sub>2</sub> following a HCHO oxidation reaction. The resulting CO<sub>2</sub> released from the reactor due to the HCHO oxidation can be analyzed online with gas chromatograph.

## 2.4. H<sub>2</sub>-temperature programmed reduction

H<sub>2</sub>-temperature programmed reduction (TPR) measurements were carried out in a U-shape quartz micro-reactor with a PX-200 catalytic characterization system equipped with a gas chromatograph. A TCD detector in a gas chromatograph was used. About 50 mg of catalyst was loaded and pretreated with high purity N<sub>2</sub> at 80 °C for 30 min. to remove the substances adsorbed on the catalyst surface. After cooling the reactor down to room temperature and introducing the reduction agent of 10% H<sub>2</sub>/N<sub>2</sub> with a flow rate of 50 mL min<sup>-1</sup>, the temperature was then programmed to rise at a ramp of 10 °C min<sup>-1</sup> to obtain the H<sub>2</sub>-TPR data.

## 2.5. Temperature programmed surface reaction

Temperature programmed surface reaction (TPSR) experiments were performed to acquire information about the adsorbed species, HCHO and O<sub>2</sub>, on the catalyst surface during the reaction. About 200 mg of catalyst was loaded into the reactor and purged with high purity He. The temperature of the reactor was increased linearly from ambient to 200 °C in order to remove the substances adsorbed on the catalyst surface. The catalyst was then cooled down to 5 °C in the flow of high purity He, following the introduction of HCHO and O<sub>2</sub> carried by purified air. The HCHO flowed through the reactor for 30 min, allowing the substances involved to adsorb on the catalyst. Subsequently, the catalysts were purged with high purity He for 30 min to remove unabsorbed substances in the reactor, and the temperature of the reactor was increased at a designed rate of 10 °C min<sup>-1</sup> in a flow of high purity He to allow the oxidation reaction to take place. The oxidation product and CO<sub>2</sub> in the effluent gas from the reactor was analyzed using the TCD detector.

# 3. Results and discussion

## 3.1. 3DOM CeO<sub>2</sub>-Co<sub>3</sub>O<sub>4</sub> supports

By infiltrating a Ce(NO<sub>3</sub>)<sub>3</sub> and Co(Ac)<sub>2</sub> precursor solution into the interstices of PS colloidal crystal arrays and removing the PS sphere templates via calcination, 3DOM CeO<sub>2</sub>-Co<sub>3</sub>O<sub>4</sub> supports with well-defined pore sizes and different Ce/Co molar ratios at 5.9:1, 4.1:1, 2.5:1, 1:1.2, 1:3.2, and 1:5.9 were achieved, as shown by their typical SEM images in Fig. 1. The CeO<sub>2</sub>-Co<sub>3</sub>O<sub>4</sub> supports exhibit well-defined 3DOM interconnected structures with average pore sizes around ~200 nm. Well-ordered colloidal templates and interconnected inorganic walls create a “honeycomb” pore structures in three dimensions, and the close packing order of the original colloidal templates is preserved in all 3DOM CeO<sub>2</sub>-Co<sub>3</sub>O<sub>4</sub> supports [32–35]. No obvious changes in pore size of the 3DOM CeO<sub>2</sub>-Co<sub>3</sub>O<sub>4</sub> supports due to the variation of Ce/Co molar ratio are detected.

## 3.2. 3DOM Au/CeO<sub>2</sub>-Co<sub>3</sub>O<sub>4</sub> catalysts

### 3.2.1. Structure of 3DOM Au/CeO<sub>2</sub>-Co<sub>3</sub>O<sub>4</sub> catalysts

3DOM Au/CeO<sub>2</sub>-Co<sub>3</sub>O<sub>4</sub> catalysts with different nominal Au loading contents were synthesized via in situ formation of active catalytic species of Au nanoparticles on 3DOM CeO<sub>2</sub>-Co<sub>3</sub>O<sub>4</sub> supports. Fig. 2 typically shows the TEM images of 3DOM ~3 wt% Au/(2.5:1)CeO<sub>2</sub>-Co<sub>3</sub>O<sub>4</sub> catalysts. The TEM image shown in Fig. 2(a) shows that the ~3 wt% Au/CeO<sub>2</sub>-Co<sub>3</sub>O<sub>4</sub> catalysts preserve the well-defined macroporous structure that is observed in the CeO<sub>2</sub>-Co<sub>3</sub>O<sub>4</sub> supports, but the uniformity of the 3DOM structure is partially destroyed. The collapse of the 3DOM skeleton in ~3 wt% Au/CeO<sub>2</sub>-Co<sub>3</sub>O<sub>4</sub> catalysts implies poor thermostability and low mechanical strength due to the destruction in basic deposition medium for loading Au nanoparticles. Interestingly, the magnified TEM image displayed in Fig. 2(b) reveals the existence of nanoporous walls in



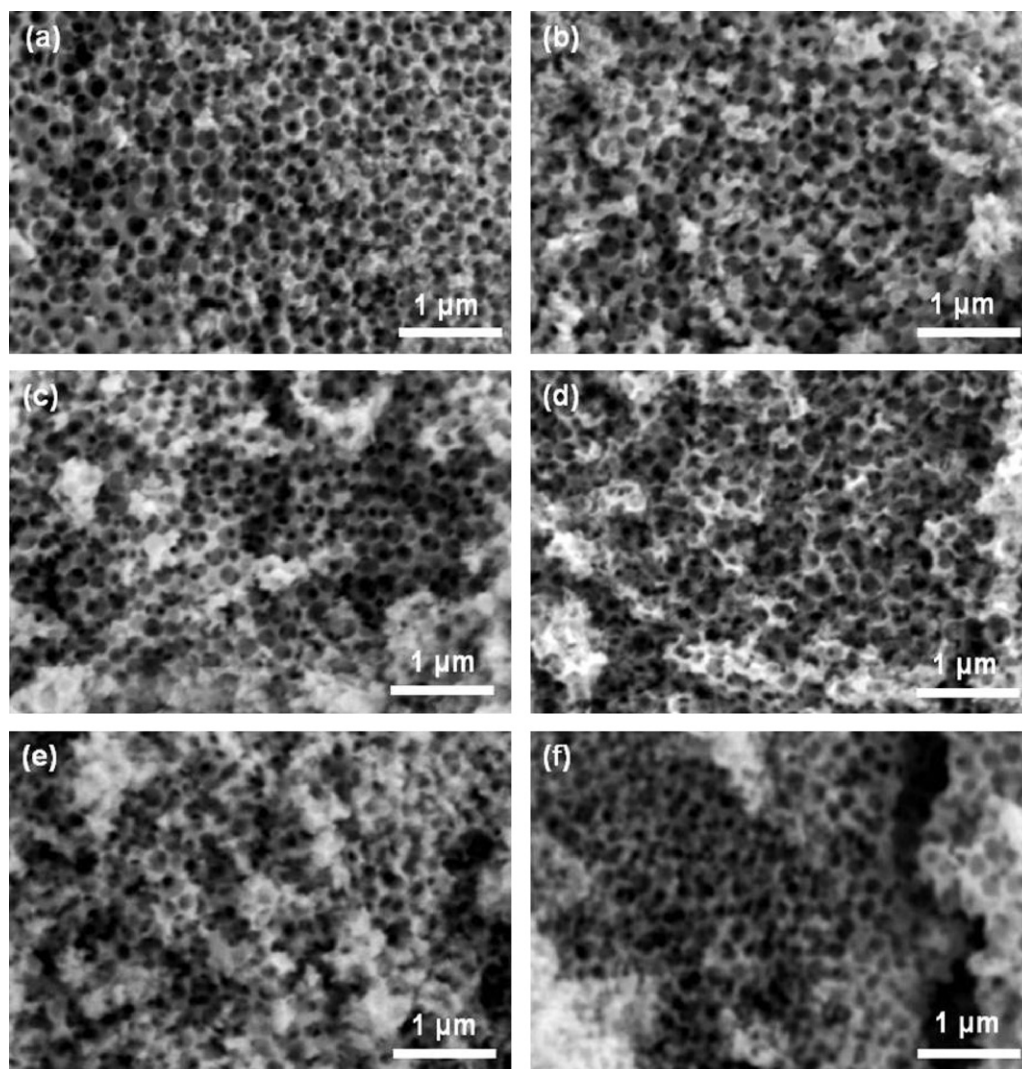


**Fig. 1.** SEM images of 3DOM  $\text{CeO}_2\text{-Co}_3\text{O}_4$  supports with various molar ratios of Ce/Co at (a) 5.9:1, (b) 4.1:1, (c) 2.5:1, (d) 1:1.2, (e) 1:3.2, and (f) 1:5.9.

the 3DOM  $\sim 3$  wt%  $\text{Au/CeO}_2\text{-Co}_3\text{O}_4$  catalysts, and the sizes of the nanopores are  $\sim 20$  nm at first glance. However, the high resolution transmission electron microscopy (HRTEM) image shown in Fig. 2(c) clearly indicates that the nanoporous walls are composed of many nanopores resulting from the aggregation of ultrafine metallic oxide nanoparticles. The sizes of the nanopores are estimated to be  $\sim 4$  nm [marked with a white circle in Fig. 2(c)]; while the ultrafine metallic oxide nanoparticles are  $\sim 5$  nm in diameter [marked with black circles in Fig. 2(c)], which are well consistent with Barrett–Joyner–Halenda (BJH) pore size and volume analysis and XRD measurements. A large amount of nanopores on the walls of the 3DOM skeleton may account for the large specific area of 3DOM  $\sim 3$  wt%  $\text{Au/CeO}_2\text{-Co}_3\text{O}_4$  in comparison to 3DOM  $\sim 3$  wt%  $\text{Au/CeO}_2$  catalysts [9]. Fig. 2(d) further proves the good crystallinity of 3DOM  $\sim 3$  wt%  $\text{Au/CeO}_2\text{-Co}_3\text{O}_4$  catalysts, and the reflection with  $d$  spacing values of 0.31 and 0.285 nm corresponding to  $\text{CeO}_2$  (1 1 1) and  $\text{Co}_3\text{O}_4$  (2 2 0) lattice planes, respectively, are clearly observed, suggesting the valence state of  $\text{Co}^{3+}$  existing on the surfaces of  $\sim 3$  wt%  $\text{Au/CeO}_2\text{-Co}_3\text{O}_4$  catalysts. The  $\text{Co}_3\text{O}_4$  with the lattice plane of (2 2 0) exposed on the catalyst surfaces is in favor of HCHO catalytic oxidation, CO oxidation, and ethylene oxidation [13,36,37]. Due to the uniform embedment of Au nanoparticles in pore canals or high dispersion in supports, no reflections related to Au species are observed in the present TEM characterization. However, the

presence of Au in the 3DOM  $\sim 3$  wt%  $\text{Au/CeO}_2\text{-Co}_3\text{O}_4$  catalysts is still firmly confirmed by energy dispersive X-ray spectroscopy (EDX) characterization (Fig. S1). The EDX measurement also gives the Ce/Co molar ratio at 2.1:1, which is very close to the Ce/Co molar ratio at 2.5:1 measured by inductively coupled plasma atomic emission spectroscopy (ICP-AES) analysis.

### 3.2.2. Composition of 3DOM $\text{Au/CeO}_2\text{-Co}_3\text{O}_4$ catalysts

The compositions of the 3DOM  $\text{Au/CeO}_2\text{-Co}_3\text{O}_4$  catalysts were measured by inductively coupled plasma mass spectrometry (ICP-MS) and inductively coupled plasma atomic emission spectrometry (ICP-AES), which could obtain the actual Au, Co, and Ce contents in the catalysts, and the results are listed in Table 1. It is revealed in Table 1 that 3DOM  $\text{Au/CeO}_2\text{-Co}_3\text{O}_4$  catalysts with various Ce/Co molar ratios can be achieved by adjusting the molar ratio and the concentration of  $\text{Ce}(\text{NO}_3)_3$  and  $\text{Co}(\text{Ac})_2$  precursor solution. When the Ce/Co molar ratio is larger than 1, which means more Ce content is incorporated into  $\text{Au/CeO}_2\text{-Co}_3\text{O}_4$  catalysts, the actual Ce and Co contents are in good agreement with the nominal Ce and Co contents. However, when the Ce/Co molar ratio is less than 1, which indicates that more Co content is included in the  $\text{Au/CeO}_2\text{-Co}_3\text{O}_4$  catalysts, the actual Ce and Co contents are deviated for the nominal Ce and Co contents. When loading Au onto such 3DOM  $\text{CeO}_2\text{-Co}_3\text{O}_4$  supports, the deviation of actual Au content from

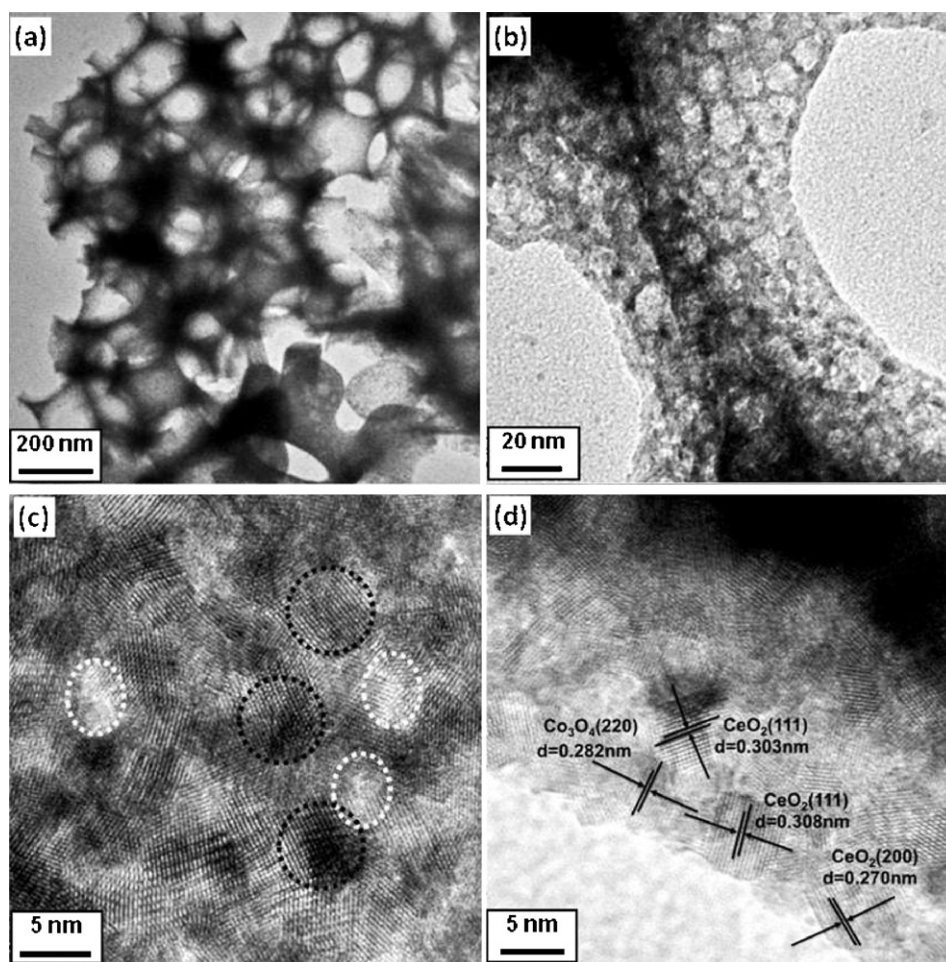


Fig. 2. TEM (a and b) and HRTEM (c and d) images of 3DOM  $\sim 3$  wt% Au/(2.5:1)CeO<sub>2</sub>-Co<sub>3</sub>O<sub>4</sub> catalysts.

nominal Au content may also occur. When the higher Ce content is incorporated into 3DOM CeO<sub>2</sub>-Co<sub>3</sub>O<sub>4</sub> supports, more Au content could be loaded. When the higher Co content exists in the 3DOM CeO<sub>2</sub>-Co<sub>3</sub>O<sub>4</sub> supports, less Au content could be loaded. This implies that Au may have stronger interaction with CeO<sub>2</sub> than Co<sub>3</sub>O<sub>4</sub> supports and mainly combines with Ce atoms in 3DOM Au/CeO<sub>2</sub>-Co<sub>3</sub>O<sub>4</sub> catalysts [38].

**Table 1**

The composition of 3DOM Au/CeO<sub>2</sub>-Co<sub>3</sub>O<sub>4</sub> catalysts estimated by ICP-MS and ICP-AES measurements.

Catalyst	Nominal content of Au (wt%)	Actual content of Au (wt%)	Nominal molar ratio of Ce/Co	Actual molar ratio of Ce/Co
3DOM Au/CeO <sub>2</sub>	3	1.38	1:0	1:0
3DOM Au/CeO <sub>2</sub> -Co <sub>3</sub> O <sub>4</sub>	3	2.15	5:1	4.8:1
	3	2.15	4:1	4.1:1
	3	2.09	3:1	3:1
	1	0.80	2:1	2.5:1
	2	1.25	2:1	2.5:1
	3	2.26	2:1	2.5:1
	4	2.77	2:1	2.5:1
	3	2.22	1:1	1:1.2
	3	1.57	1:2	1:2.6
	3	1.99	1:3	1:3.2
	3	1.62	1:4	1:3.3
	3	1.82	1:5	1:3.2
3DOM Au/Co <sub>3</sub> O <sub>4</sub>	3	0.48	0:1	0:1

### 3.2.3. Surface area and porous structure of 3DOM Au/CeO<sub>2</sub>-Co<sub>3</sub>O<sub>4</sub> catalysts

To estimate the surface area and porous structure of 3DOM Au/CeO<sub>2</sub>-Co<sub>3</sub>O<sub>4</sub> catalysts, BET and BJH measurements were performed, and the results are shown in Fig. 3 and Table 2. The BET measurement displayed in Fig. 3(A) for 3DOM Au/CeO<sub>2</sub>-Co<sub>3</sub>O<sub>4</sub> catalysts shows the Type IV isotherm curves. Their narrow hysteresis loops exhibit a typical pattern of Type IV at a relative pressure from 0.4 to 1.0, indicating that 3DOM Au/CeO<sub>2</sub>-Co<sub>3</sub>O<sub>4</sub> catalysts possess mesoporous structures and confirming the 3DOM structure of Au/CeO<sub>2</sub>-Co<sub>3</sub>O<sub>4</sub> catalysts with nanoporous walls. The corresponding pore size distribution shown in Fig. 3(B) indicates that the pore sizes of 3DOM Au/CeO<sub>2</sub>-Co<sub>3</sub>O<sub>4</sub> catalysts are dominantly distributed between 3.0 nm and 4.2 nm with a peak value at 3.8 nm, which is in good agreement with TEM measurement.

**Table 2**

The BET and BJH properties of 3DOM CeO<sub>2</sub>-Co<sub>3</sub>O<sub>4</sub> supports and Au/CeO<sub>2</sub>-Co<sub>3</sub>O<sub>4</sub> catalysts.

Supports and catalysts	S <sub>BET</sub> (m <sup>2</sup> /g)	V <sub>p</sub> (cm <sup>3</sup> /g)	D <sub>p</sub> (nm)
3DOM CeO <sub>2</sub>	60	0.17	–
3DOM $\sim 3$ wt% Au/CeO <sub>2</sub>	52	0.15	–
3DOM (5.9:1)CeO <sub>2</sub> -Co <sub>3</sub> O <sub>4</sub>	72	0.091	3.8
3DOM $\sim 3$ wt% Au/(5.9:1)CeO <sub>2</sub> -Co <sub>3</sub> O <sub>4</sub>	53	0.089	3.6
3DOM (2.5:1)CeO <sub>2</sub> -Co <sub>3</sub> O <sub>4</sub>	70	0.094	3.7
3DOM $\sim 3$ wt% Au/(2.5:1)CeO <sub>2</sub> -Co <sub>3</sub> O <sub>4</sub>	54	0.075	3.6
3DOM (1:3.2)CeO <sub>2</sub> -Co <sub>3</sub> O <sub>4</sub>	45	0.13	3.6
3DOM $\sim 3$ wt% Au/(1:3.2)CeO <sub>2</sub> -Co <sub>3</sub> O <sub>4</sub>	41	0.12	3.4

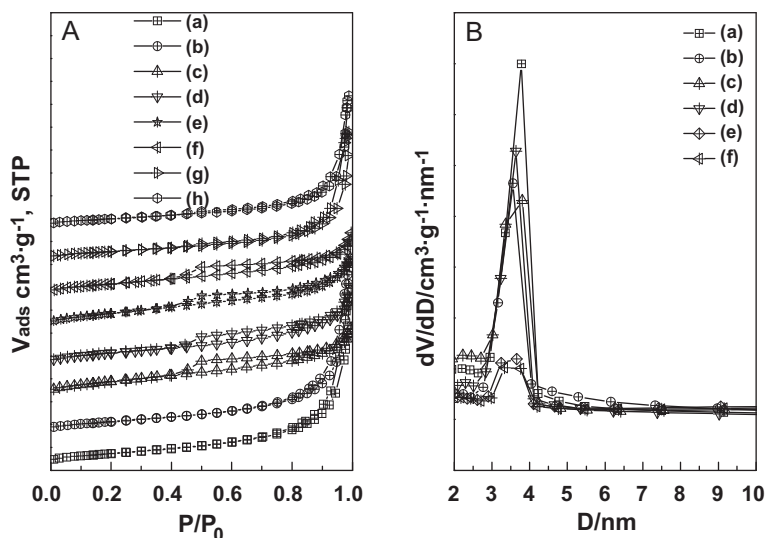


**Fig. 3.** (A) N<sub>2</sub> adsorption-desorption isotherms of 3DOM (a) CeO<sub>2</sub>, (b) Au/CeO<sub>2</sub>, (c) (5.9:1)CeO<sub>2</sub>-Co<sub>3</sub>O<sub>4</sub>, (d) Au/(5.9:1)CeO<sub>2</sub>-Co<sub>3</sub>O<sub>4</sub>, (e) (2.5:1)CeO<sub>2</sub>-Co<sub>3</sub>O<sub>4</sub>, (f) Au/(2.5:1)CeO<sub>2</sub>-Co<sub>3</sub>O<sub>4</sub>, (g) (1:3.2)CeO<sub>2</sub>-Co<sub>3</sub>O<sub>4</sub>, and (h) Au/(1:3.2)CeO<sub>2</sub>-Co<sub>3</sub>O<sub>4</sub>, and (B) BJH measurements of 3DOM (a) (5.9:1)CeO<sub>2</sub>-Co<sub>3</sub>O<sub>4</sub>, (b) Au/(5.9:1)CeO<sub>2</sub>-Co<sub>3</sub>O<sub>4</sub>, (c) (2.5:1)CeO<sub>2</sub>-Co<sub>3</sub>O<sub>4</sub>, (d) Au/(2.5:1)CeO<sub>2</sub>-Co<sub>3</sub>O<sub>4</sub>, (e) (1:3.2)CeO<sub>2</sub>-Co<sub>3</sub>O<sub>4</sub>, and (f) Au/(1:3.2)CeO<sub>2</sub>-Co<sub>3</sub>O<sub>4</sub>.

### 3.2.4. XRD

To further study the phase structure of 3DOM Au/CeO<sub>2</sub>-Co<sub>3</sub>O<sub>4</sub> catalysts, XRD measurements were carried out. Fig. 4 shows a series of XRD patterns of 3DOM ~3 wt% Au/CeO<sub>2</sub>-Co<sub>3</sub>O<sub>4</sub> catalysts with various Ce/Co molar ratios at 0:1, 1:5.9, 1:3.2, 1:2.6, 2.5:1, 4.1:1, 5.9:1, and 1:0. It is found that the fluorite phase corresponding to CeO<sub>2</sub> is observed in 3DOM ~3 wt% Au/CeO<sub>2</sub> catalyst, and the spinel phase indexed to Co<sub>3</sub>O<sub>4</sub> is detected in 3DOM ~3 wt% Au/Co<sub>3</sub>O<sub>4</sub> catalyst. Both fluorite and spinel phases corresponding to CeO<sub>2</sub> and Co<sub>3</sub>O<sub>4</sub> are viewed simultaneously in 3DOM 3 wt% Au/CeO<sub>2</sub>-Co<sub>3</sub>O<sub>4</sub> catalysts with Ce/Co molar ratios at 1:5.9, 1:3.2, 1:2.6, 2.5:1, 4.1:1, and 5.9:1, indicating the co-existence of CeO<sub>2</sub> and Co<sub>3</sub>O<sub>4</sub>. Furthermore, when the Co content is lower, only fluorite phased CeO<sub>2</sub> is found, which suggests that Co ions are probably incorporated into the CeO<sub>2</sub> lattice and lead to the formation of CeO<sub>2</sub>-Co<sub>3</sub>O<sub>4</sub> solid solution by considering the fact that the ionic radius of Co<sup>3+</sup> (0.063 nm) and Co<sup>2+</sup> (0.065 nm) is smaller than that of Ce<sup>4+</sup> (0.094 nm), which was also proven by the decrease of lattice parameters of CeO<sub>2</sub> with the increase of Co doping contents, as shown in Table 3. The mean particle sizes and phase structures of CeO<sub>2</sub> and Co<sub>3</sub>O<sub>4</sub> in 3DOM ~3 wt% Au/CeO<sub>2</sub> and Co<sub>3</sub>O<sub>4</sub> catalysts deduced from XRD

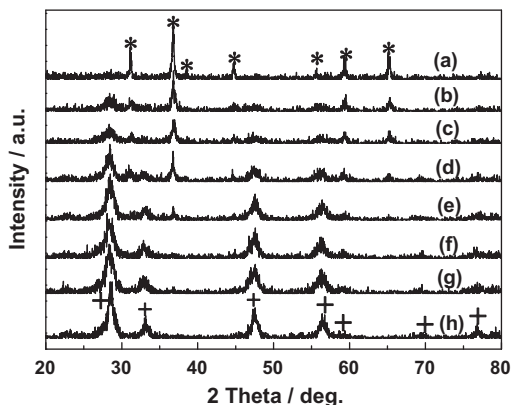


**Fig. 4.** XRD patterns of 3DOM ~3 wt% Au/CeO<sub>2</sub>-Co<sub>3</sub>O<sub>4</sub> catalysts with various Ce/Co molar ratios at (a) 0:1, (b) 1:5.9, (c) 1:3.2, (d) 1:2.6, (e) 2.5:1, (f) 4.1:1, (g) 5.9:1, and (h) 1:0. '\*' stands for the crystalline phase of Co<sub>3</sub>O<sub>4</sub>, and '+' refers to the crystalline phase of CeO<sub>2</sub>.

measurements are listed in Table 3. As the Co content increases, the phase separation phenomenon appears causing both spinel phased Co<sub>3</sub>O<sub>4</sub> and fluorite phased CeO<sub>2</sub> to be present in the 3DOM ~3 wt% Au/CeO<sub>2</sub>-Co<sub>3</sub>O<sub>4</sub> and causing the diffraction peaks to broaden, indicating the decrease of the crystallite sizes, which is similar to the previous report.[39]

The CeO<sub>2</sub> and Co<sub>3</sub>O<sub>4</sub> crystallite sizes in 3DOM Au/CeO<sub>2</sub> and Au/Co<sub>3</sub>O<sub>4</sub> estimated from the half-width of broadening diffraction peaks of CeO<sub>2</sub> (1 1 1) and Co<sub>3</sub>O<sub>4</sub> (3 1 1) by the Scherrer Equation are ~9.2 and ~25.8 nm, respectively. However, when incorporating Co<sup>3+</sup> into CeO<sub>2</sub>, the CeO<sub>2</sub> and Co<sub>3</sub>O<sub>4</sub> crystallite sizes in 3DOM Au/CeO<sub>2</sub>-Co<sub>3</sub>O<sub>4</sub> are much smaller than those in the corresponding Au/CeO<sub>2</sub> and Au/Co<sub>3</sub>O<sub>4</sub>. No diffraction peaks indexed to Au species are detected in the catalysts, indicating that Au species exist in the nanoparticle form and are uniformly dispersed on CeO<sub>2</sub>-Co<sub>3</sub>O<sub>4</sub> supports.

It is reported that the addition of Ce<sup>3+</sup> into Co<sub>3</sub>O<sub>4</sub> is greatly beneficial to avoid extensive sintering of Co<sub>3</sub>O<sub>4</sub> [38–40]. A similar phenomenon happens when incorporating Co<sup>3+</sup> into CeO<sub>2</sub> [41,42]. Among all 3DOM Au/CeO<sub>2</sub>-Co<sub>3</sub>O<sub>4</sub> catalysts, the 3DOM Au/CeO<sub>2</sub>-Co<sub>3</sub>O<sub>4</sub> prepared with a Ce/Co molar ratio of 2.5:1 gives the smallest crystallite sizes around 5.0 nm for CeO<sub>2</sub> and 10.2 nm for Co<sub>3</sub>O<sub>4</sub>, implying that there may be a suitable Ce/Co molar ratio for obtaining 3DOM Au/CeO<sub>2</sub>-Co<sub>3</sub>O<sub>4</sub> catalysts with the smallest crystallite sizes that may show higher surface area and catalytic activity.

### 3.2.5. XPS

The XPS measurements were carried out to quantitatively analyze the binding energy of Au 4f<sub>7/2</sub>, Co 2p<sub>3/2</sub>, and Ce 3d<sub>5/2</sub>; the content of Au and Au<sup>3+</sup>; and the molar ratios of Ce/Co, Au/Co, and Au/Ce on the surface of 3DOM Au/CeO<sub>2</sub>-Co<sub>3</sub>O<sub>4</sub> catalysts. Fig. 5 displays the experimental and fitted XPS spectra of Au 4f of 3DOM ~3 wt% Au/CeO<sub>2</sub>, Au/(2.5:1)CeO<sub>2</sub>-Co<sub>3</sub>O<sub>4</sub>, Au/(1:3.2)CeO<sub>2</sub>-Co<sub>3</sub>O<sub>4</sub>, and Au/Co<sub>3</sub>O<sub>4</sub> catalysts, and the detailed XPS results are summarized in Table 4. The Au 4f spectra indicate that both metallic and ionic Au species are present in 3DOM ~3 wt% Au/CeO<sub>2</sub>, Au/(2.5:1)CeO<sub>2</sub>-Co<sub>3</sub>O<sub>4</sub>, Au/(1:3.2)CeO<sub>2</sub>-Co<sub>3</sub>O<sub>4</sub>, and Au/Co<sub>3</sub>O<sub>4</sub> catalysts. The XPS peaks at 84.0 ± 0.2 and 87.5 ± 0.2 eV are the typical binding energy values of metallic Au [43–45], and the position of Au 4f<sub>7/2</sub> with binding energy at 85.8 ± 0.5 eV is assigned to Au<sup>3+</sup> [12,46]. This is different from literature reports that Au<sup>δ+</sup> exists in



**Table 3**Mean particle sizes and phase structures of CeO<sub>2</sub> and Co<sub>3</sub>O<sub>4</sub> nanoparticles in 3DOM ~3 wt% Au/CeO<sub>2</sub>-Co<sub>3</sub>O<sub>4</sub> catalysts.

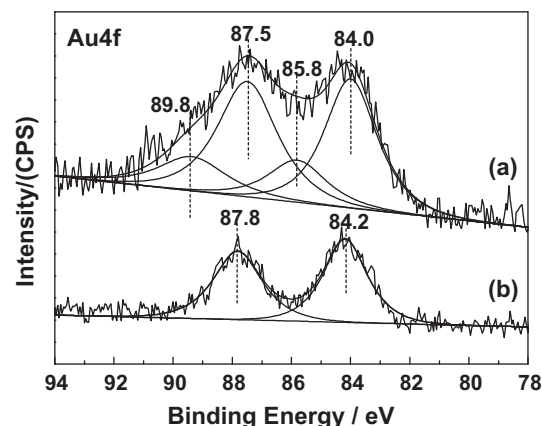
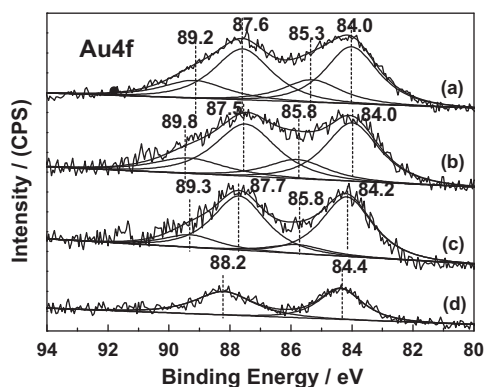
Catalysts	<i>d</i> <sub>CeO<sub>2</sub></sub> (nm)	<i>d</i> <sub>Co<sub>3</sub>O<sub>4</sub></sub> (nm)	Lattice parameters (nm)	Crystal phases
3DOM ~3 wt% Au/Co <sub>3</sub> O <sub>4</sub>	–	25.8	–	Spinel
3DOM ~3 wt% Au/(1:5.9)CeO <sub>2</sub> -Co <sub>3</sub> O <sub>4</sub>	5.8	19.2	–	Spinel, fluorite
3DOM ~3 wt% Au/(1:3.2)CeO <sub>2</sub> -Co <sub>3</sub> O <sub>4</sub>	6.0	14.4	0.5384	Spinel, fluorite
3DOM ~3 wt% Au/(1:2.5)CeO <sub>2</sub> -Co <sub>3</sub> O <sub>4</sub>	7.4	12.4	0.5389	Spinel, fluorite
3DOM ~3 wt% Au/(2.5:1)CeO <sub>2</sub> -Co <sub>3</sub> O <sub>4</sub>	5.0	10.2	0.5399	Spinel, fluorite
3DOM ~3 wt% Au/(3.2:1)CeO <sub>2</sub> -Co <sub>3</sub> O <sub>4</sub>	6.2	–	0.5402	Fluorite
3DOM ~3 wt% Au/(5.9:1)CeO <sub>2</sub> -Co <sub>3</sub> O <sub>4</sub>	7.9	–	0.5408	Fluorite
3DOM ~3 wt% Au/CeO <sub>2</sub>	9.2	–	0.5412	Fluorite

**Table 4**XPS data for evaluation of the valence states of Au, Co and Ce, and the content of Au, Co, and Ce on surface of ~3 wt% Au/CeO<sub>2</sub>-Co<sub>3</sub>O<sub>4</sub> catalysts.

Catalyst	Au 4f7/2 (eV)	Co 2p3/2 (eV)	Ce 3d5/2 (eV)	Au (wt %)	Au <sup>3+</sup> /Au	Ce/Co		Au/Ce	Au/Co
						XPS	ICP-AES		
3DOM 3 wt% Au/CeO <sub>2</sub>	84.0 85.3	–	883.2	2.04	0.43	–	–	0.085	–
3DOM 3 wt% Au/(5.9:1)CeO <sub>2</sub> -Co <sub>3</sub> O <sub>4</sub>	84.3 86.0	780.2	882.9	0.96	0.41	8.0	6.0	0.043	0.35
3DOM 3 wt% Au/(2.5:1)CeO <sub>2</sub> -Co <sub>3</sub> O <sub>4</sub>	84.0 85.8	780.2	882.9	0.92	0.36	4.6	2.5	0.045	0.21
3DOM 3 wt% Au/(1:3.2)CeO <sub>2</sub> -Co <sub>3</sub> O <sub>4</sub>	84.2 85.8	780.4	883.0	0.59	0.15	0.36	0.32	0.097	0.025
3DOM 3 wt% Au/Co <sub>3</sub> O <sub>4</sub>	84.4	780.5	–	0.44	–	–	–	–	0.017

the Au/CeO<sub>2</sub>-Co<sub>3</sub>O<sub>4</sub> catalysts [43,47]. However, only metallic Au is observed in the 3DOM Au/Co<sub>3</sub>O<sub>4</sub> catalyst. It is found that the Au content gradually increases along with the increase of Ce content in 3DOM Au/CeO<sub>2</sub>-Co<sub>3</sub>O<sub>4</sub> catalysts. Moreover, the molar ratio of Au<sup>3+</sup>/Au also rises with the increase of Ce content. This suggests that Au mainly prefers to combine with CeO<sub>2</sub>, rather than bond to Co<sub>3</sub>O<sub>4</sub>. Therefore, it is deduced that the strong interaction between Au and CeO<sub>2</sub> exists, as was previously demonstrated [43,48–50]. It is found that the actual Ce/Co molar ratio is higher than the nominal molar ratio of Ce/Co in the surface of catalysts [41,51,52]. The molar ratio of Au/Ce is much smaller than Au/Co, which also proves that the Ce prefers to migrate to the surface of the supports. The results are in good agreement with ICP-MS and ICP-AES characterizations.

Fig. 6 presents the experimental and fitted XPS spectra of the fresh and deactivated 3DOM ~3 wt% Au/(2.5:1)CeO<sub>2</sub>-Co<sub>3</sub>O<sub>4</sub> catalysts, and the detailed XPS results are summarized in Table 5. It is obvious that both metallic and ionic Au species are present in the fresh 3DOM ~3 wt% Au/(2.5:1)CeO<sub>2</sub>-Co<sub>3</sub>O<sub>4</sub> catalyst; however, only

**Fig. 6.** Experimental and fitted XPS spectra of Au 4f of the fresh and deactivated 3DOM ~3 wt% Au/(2.5:1)CeO<sub>2</sub>-Co<sub>3</sub>O<sub>4</sub> catalysts.**Fig. 5.** Experimental and fitted XPS spectra of Au 4f of 3DOM (a) ~3 wt% Au/CeO<sub>2</sub>, (b) ~3 wt% Au/(2.5:1)CeO<sub>2</sub>-Co<sub>3</sub>O<sub>4</sub>, (c) ~3 wt% Au/(1:3.2)CeO<sub>2</sub>-Co<sub>3</sub>O<sub>4</sub>, and (d) ~3 wt% Au/Co<sub>3</sub>O<sub>4</sub> catalysts.

metallic Au is detected in the deactivated catalyst, which is similar to the previous report [47]. Therefore, it is deduced that the interaction between Au and the support becomes weaker in the deactivated catalyst. The surface concentration of Au, designating as the atomic ratio of Au to the total metal atoms, measured by XPS is about 0.92% in the fresh catalysts and 0.64% in the deactivated catalysts. Both are lower than the bulk Au concentration (2.04%). The Ce/Co atomic ratios at the catalyst surface are 4.6 for the fresh catalyst and 3.9 for the deactivated one, remarkably higher than

**Table 5**XPS data for evaluation of the valence states of Co and Ce, and the molar ratio of Ce/Co and Au<sup>3+</sup>/Au on surface of the fresh and deactivated 3DOM ~3 wt% Au/(2.5:1)CeO<sub>2</sub>-Co<sub>3</sub>O<sub>4</sub> catalysts.

Catalysts	Binding energy (eV)				Ce/Co	Au (%)	Au <sup>3+</sup> /Au
	Co 2p3/2	Co 2p1/2	ΔE	Ce 3d5/2			
Fresh	780.3	795.5	15.2	882.9	4.6	0.92	0.36
Deactivated	780.5	796.3	15.8	883.1	3.9	0.64	0

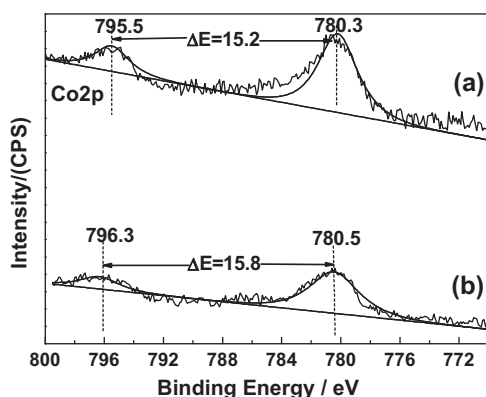


Fig. 7. Experimental and fitted XPS spectra of Co 2p of the fresh and deactivated 3DOM 3 wt% Au/(2.5:1)CeO<sub>2</sub>-Co<sub>3</sub>O<sub>4</sub> catalysts.

the nominal value at 2.5 in catalyst bulk. The increase of the Ce/Co atomic ratio suggests that the surface is Ce-rich, which is consistent with the results of HRTEM. Compared to that of the fresh catalyst, the surface Ce/Co atomic ratio of the used catalyst is decreased, indicating that the Ce-rich oxide structure is reordered [53].

Fig. 7 shows the experimental and fitted XPS spectra of Co 2p of the fresh and deactivated 3DOM 3 wt% Au/(2.5:1)CeO<sub>2</sub>-Co<sub>3</sub>O<sub>4</sub> catalysts. According to the reports [41,54], the oxidation state of Co can be distinguished by the spin-orbit splitting of the Co 2p peaks ( $\Delta E$ ). The value of  $\Delta E$  is 16.0 eV for CoO, 15.0 eV for Co<sub>3</sub>O<sub>4</sub>, and 15.2 eV for mixed-valence Co<sub>3</sub>O<sub>4</sub>. The  $\Delta E$  values of the Co 2p features in the fresh and deactivated 3DOM Au/CeO<sub>2</sub>-Co<sub>3</sub>O<sub>4</sub> catalysts clearly indicate that Co<sub>3</sub>O<sub>4</sub> is the main phase on the surface of the fresh catalyst, but CoO emerges dominantly on the surface of the deactivated catalyst, even though CoO is not discovered in XRD (Fig. S2). The increase of CoO means a weakness of the interaction between CoO and CeO<sub>2</sub>, which leads to the decrease of oxygen vacancies. TEM characterization (Fig. S3) of the deactivated 3DOM ~3 wt% Au/(2.5:1) CeO<sub>2</sub>-Co<sub>3</sub>O<sub>4</sub> catalysts further confirms similar results. It is indicated that besides the observation of lattice planes of (1 1 1) and (2 2 0) corresponding to fluorite phased CeO<sub>2</sub>, the reflection with a  $d$  spacing of 0.246 nm indexed to the CoO (1 0 1) plane is observed in the deactivated 3DOM ~Au 3 wt%/(2.5:1) CeO<sub>2</sub>-Co<sub>3</sub>O<sub>4</sub> catalyst, indicating that Co<sub>3</sub>O<sub>4</sub> participates in the HCHO oxidation, and is reduced from Co<sub>3</sub>O<sub>4</sub> into CoO. The existence of Co<sup>3+</sup> may account for the enhanced catalytic activity of 3DOM ~3 wt% Au/(2.5:1) CeO<sub>2</sub>-Co<sub>3</sub>O<sub>4</sub> catalysts.

The experimental and fitted XPS spectra of O 1s of the fresh and deactivated 3DOM ~3 wt% Au/(2.5:1)CeO<sub>2</sub>-Co<sub>3</sub>O<sub>4</sub> catalysts can be fitted into three binding energy peaks (Fig. S4). The lower binding energy band at 529–530 eV corresponds to O<sup>2-</sup> of CeO<sub>2</sub> and Co<sub>3</sub>O<sub>4</sub>, and the higher binding energy band at 531–532 eV is indexed to O<sup>2-</sup> of the surface carbonates and hydroxides of Ce and Co [25]. Compared to that of the deactivated catalysts, the O<sup>2-</sup> peak of the fresh catalyst slightly shifts to a higher binding energy value [53]. Due to the fact that the surface Ce/Co atomic ratio decreases in the used catalysts, the low contribution of oxygen leads to the increase of O 1s binding energy.

### 3.3. Catalytic performance of HCHO oxidation

#### 3.3.1. Catalytic property of 3 DOM Au/CeO<sub>2</sub>-Co<sub>3</sub>O<sub>4</sub> catalysts

The reaction intermediates and products of HCHO catalytic oxidation over 3 DOM Au/CeO<sub>2</sub>-Co<sub>3</sub>O<sub>4</sub> catalysts were online monitored by GC. It was found that the chromatograph peaks indexed to air, CO<sub>2</sub>, HCHO, H<sub>2</sub>O, CH<sub>3</sub>OH, and HCOOH are obviously detected. The air, HCHO and CH<sub>3</sub>OH peaks appearing in GC diagrams are arisen from the original feeding gaseous stream [55]. The CO<sub>2</sub> and

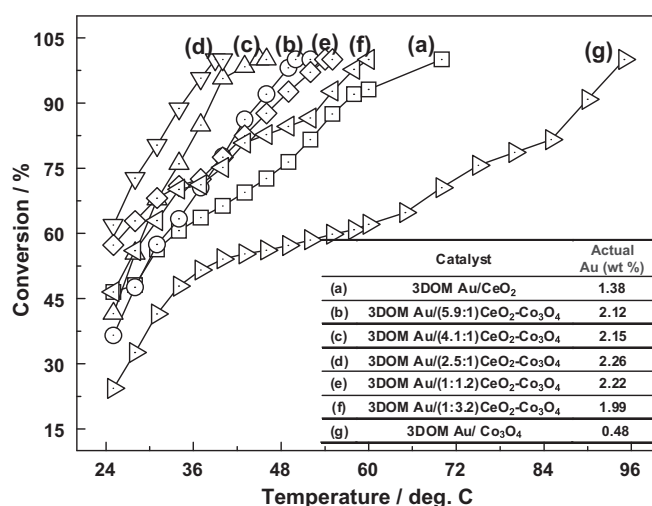
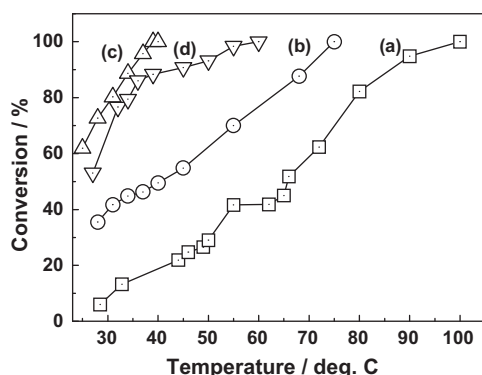


Fig. 8. Catalytic activity of 3DOM (a) Au/CeO<sub>2</sub>, (b) Au/(5.9:1)CeO<sub>2</sub>-Co<sub>3</sub>O<sub>4</sub>, (c) Au/(4.1:1)CeO<sub>2</sub>-Co<sub>3</sub>O<sub>4</sub>, (d) Au/(2.5:1)CeO<sub>2</sub>-Co<sub>3</sub>O<sub>4</sub>, (e) Au/(1:1.2)CeO<sub>2</sub>-Co<sub>3</sub>O<sub>4</sub>, (f) Au/(1:3.2)CeO<sub>2</sub>-Co<sub>3</sub>O<sub>4</sub>, and (g) Au/Co<sub>3</sub>O<sub>4</sub> catalysts for HCHO oxidation. The actual Au contents corresponding to each catalyst were provided in the inset of the figure.

H<sub>2</sub>O are the reaction products of the catalytic oxidation of HCHO. The HCOOH is estimated to be the reaction intermediate of HCHO catalytic oxidation over 3DOM Au/CeO<sub>2</sub>-Co<sub>3</sub>O<sub>4</sub> catalysts, which was also evidenced in previous reports [55].

The catalytic activity of 3DOM CeO<sub>2</sub>-Co<sub>3</sub>O<sub>4</sub> supports with different Ce/Co molar ratios at 5.9:1, 3.2:1, 2.5:1, 1:1.2, 1:3.2, and 1:5.9 for HCHO oxidation under various temperatures was tested. The catalytic activity of 3DOM CeO<sub>2</sub>-Co<sub>3</sub>O<sub>4</sub> supports is quite inactive at low temperature (Fig. S6). The lowest temperature for HCHO complete conversion is around ~145 °C. However, after loading Au onto CeO<sub>2</sub>-Co<sub>3</sub>O<sub>4</sub> supports, the catalytic activity is largely improved. Fig. 8 shows the catalytic activity of 3DOM ~3 wt% Au/CeO<sub>2</sub>-Co<sub>3</sub>O<sub>4</sub> catalysts with different Ce/Co molar ratios at 5.9:1, 3.2:1, 2.5:1, 1:1.2, 1:3.2, 1:5.9 for HCHO oxidation under various testing temperatures. It can be clearly seen that after loading the catalytic species of Au, the temperature for complete conversion of HCHO into CO<sub>2</sub> and H<sub>2</sub>O over 3DOM ~3 wt% Au/CeO<sub>2</sub>-Co<sub>3</sub>O<sub>4</sub> catalysts is dramatically decreased in comparison to the corresponding 3DOM CeO<sub>2</sub>-Co<sub>3</sub>O<sub>4</sub> supports. Among all the investigated catalysts with different molar ratios of Ce/Co, the 3DOM ~3 wt% Au/(2.5:1) CeO<sub>2</sub>-Co<sub>3</sub>O<sub>4</sub> catalyst shows the lowest mass-specific rates of  $6.63 \times 10^{-4} \text{ mol h}^{-1} \text{ g}^{-1} \text{ Au}$  and the highest TOF of  $0.53 \text{ h}^{-1}$  (Table S2), suggesting that the 3DOM ~3 wt% Au/(2.5:1) CeO<sub>2</sub>-Co<sub>3</sub>O<sub>4</sub> catalyst has the highest catalytic activity. The temperature for complete conversion of HCHO over 3DOM ~3 wt% Au/(2.5:1)CeO<sub>2</sub>-Co<sub>3</sub>O<sub>4</sub> catalyst can be reduced to 39 °C. Since the amount of actual loaded on Au ~3 wt% Au/(2.5:1)CeO<sub>2</sub>-Co<sub>3</sub>O<sub>4</sub> catalysts is at 2.26% according to the ICP-AES measurements, the highest among all Au/(2.5:1)CeO<sub>2</sub>-Co<sub>3</sub>O<sub>4</sub> catalysts with different Ce/Co molar ratios at 5.9:1, 3.2:1, 2.5:1, 1:1.2, 1:3.2, 1:5.9, which mainly account for the achievement of the highest catalytic activity. Comparatively, the catalytic temperatures for complete conversion of HCHO over pure 3DOM ~3 wt% Au/CeO<sub>2</sub> and ~3 wt% Au/Co<sub>3</sub>O<sub>4</sub> catalysts are around 75 °C and 95 °C, respectively. This indicates that by using CeO<sub>2</sub>-Co<sub>3</sub>O<sub>4</sub> nanocomposite as a support, the catalytic activity of 3DOM Au/CeO<sub>2</sub>-Co<sub>3</sub>O<sub>4</sub> catalyst can be dramatically increased. The catalytic activity of 3DOM Au/CeO<sub>2</sub>-Co<sub>3</sub>O<sub>4</sub> catalysts with different Ce/Co molar ratios is increased initially and decreased subsequently with increasing Ce/Co molar ratios. The highest catalytic activity can be realized in 3DOM ~3 wt% Au/(2.5:1)CeO<sub>2</sub>-Co<sub>3</sub>O<sub>4</sub> catalyst, with 61% HCHO conversion rate at room temperature and 100% HCHO conversion rate at 39 °C. This





**Fig. 9.** Comparison of catalytic activity of 3DOM Au/(2.5:1)CeO<sub>2</sub>-Co<sub>3</sub>O<sub>4</sub> catalysts with various theoretical Au loading contents on HCHO oxidation: (a) ~1, (b) ~2, (c) ~3, and (d) ~4 wt%.

suggests that the Ce-enriched support has better catalytic activity than the Co-enriched support when using CeO<sub>2</sub>-Co<sub>3</sub>O<sub>4</sub> nanocomposite as a support for Au loading for catalytic oxidation of HCHO.

To investigate the influences of Au loading contents on their catalytic activity, 3DOM Au/(2.5:1)CeO<sub>2</sub>-Co<sub>3</sub>O<sub>4</sub> catalysts with different nominal Au loading contents were prepared for the HCHO catalytic oxidation test. Fig. 9 shows the catalytic activity of HCHO catalytic oxidation over 3DOM Au/(2.5:1)CeO<sub>2</sub>-Co<sub>3</sub>O<sub>4</sub> catalyst (80 nm pore size) with nominal Au loading contents of ~1, ~2, ~3, and ~4 wt%. It is shown that 3DOM Au/(2.5:1)CeO<sub>2</sub>-Co<sub>3</sub>O<sub>4</sub> catalyst with nominal Au loading content at ~3 wt% possesses the highest efficient catalytic activity of HCHO oxidation with 61% conversion rate at room temperature and 100% conversion rate at 39 °C. The ICP-MS characterization (Table 1) shows that the actual Au loading content in this catalyst is ~2.26 wt%. Further increasing the Au loading content to ~4 wt% (actual content at ~2.77 wt%) in catalysts may cause the decrease of catalytic activity due to the aggregation of Au nanoparticles.

As the Au/CeO<sub>2</sub>-Co<sub>3</sub>O<sub>4</sub> catalysts prepared in this work possess 3DOM structures, the pore sizes of 3DOM Au/CeO<sub>2</sub>-Co<sub>3</sub>O<sub>4</sub> catalyst may have profound effects on the catalytic activity for HCHO oxidation. Thus, the catalytic activity of 3DOM Au ~3 wt%/(2.5:1)CeO<sub>2</sub>-Co<sub>3</sub>O<sub>4</sub> catalysts with 80, 130, and 240 nm pore sizes were comparatively studied, and their catalytic performance curves are displayed in Fig. 10. It can be seen from Fig. 10 that the 3DOM Au ~3 wt%/(2.5:1)CeO<sub>2</sub>-Co<sub>3</sub>O<sub>4</sub> with 80 nm pores displays the highest catalytic activity for HCHO oxidation, as it has the highest surface area, and the small pore size may lead to more uniform distribution of small Au nanoparticles, which may account for the improvement of catalytic capability.

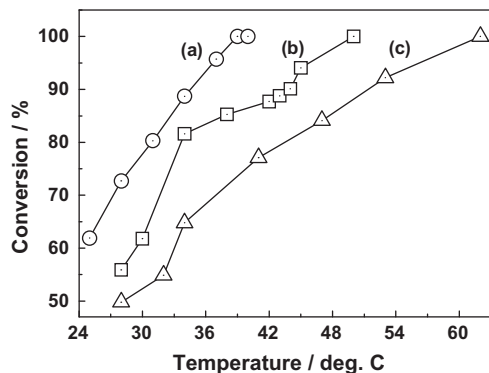


**Fig. 10.** Comparison of catalytic activity of ~3 wt% Au/(2.5:1)CeO<sub>2</sub>-Co<sub>3</sub>O<sub>4</sub> catalysts with different pore sizes for HCHO oxidation: (a) 80, (b) 130, and (c) 240 nm.

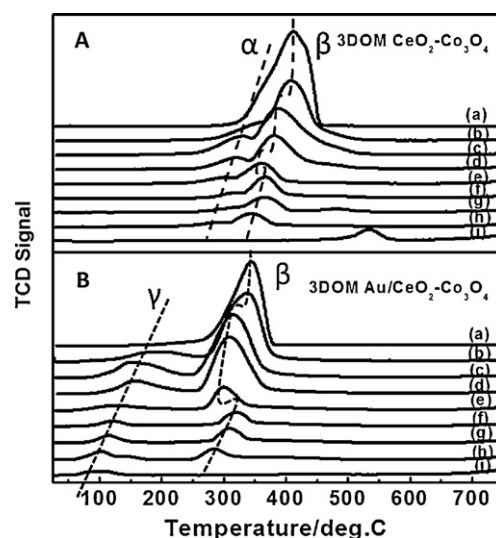


**Fig. 11.** H<sub>2</sub>-TPR profiles of (A) 3DOM CeO<sub>2</sub>-Co<sub>3</sub>O<sub>4</sub> supports and (B) ~3 wt% Au/CeO<sub>2</sub>-Co<sub>3</sub>O<sub>4</sub> catalysts (B) with various different Ce/Co atomic ratio at (a) 0 (pure Co<sub>3</sub>O<sub>4</sub>), (b) 1:5.9, (c) 1:3.2, (d) 1:1.2, (e) 2.5:1, (f) 4.1:1, (g) 4.8:1, (h) 5.9:1, and (i) 1 (pure CeO<sub>2</sub>).

The catalytic stability of 3DOM Au/CeO<sub>2</sub>-Co<sub>3</sub>O<sub>4</sub> catalysts was also evaluated by carrying out the catalytic performance of 3DOM Au ~3 wt%/CeO<sub>2</sub>-Co<sub>3</sub>O<sub>4</sub> catalyst in time-on-stream for 50 h (Fig. S7). The deactivation of the catalyst during this period did not occur, implying that the 3DOM ~3 wt% Au/(2.5:1)CeO<sub>2</sub>-Co<sub>3</sub>O<sub>4</sub> catalyst shows the catalytic stability with 100% conversion rate of HCHO oxidation at 50 °C in a continuous reaction period of 50 h. The catalytic stability of the 3DOM ~3 wt% Au/(2.5:1)CeO<sub>2</sub>-Co<sub>3</sub>O<sub>4</sub> catalyst was also estimated by carrying out the catalytic performance of 3DOM ~3 wt% Au/(2.5:1)CeO<sub>2</sub>-Co<sub>3</sub>O<sub>4</sub> catalyst with five testing cycles. It was found that the 3DOM ~3 wt% Au/(2.5:1)CeO<sub>2</sub>-Co<sub>3</sub>O<sub>4</sub> catalyst showed relatively stable catalytic performances with 100% conversion of HCHO oxidation at the temperature in 39–50 °C. The temperature for 100% conversion of HCHO oxidation for the fresh catalyst kept at 39 °C, but with a little fluctuation between 39 °C and 50 °C for the repeated catalysts, suggesting the catalytic stability of ~3 wt% Au/(2.5:1)CeO<sub>2</sub>-Co<sub>3</sub>O<sub>4</sub>.

### 3.4. Catalytic mechanism

#### 3.4.1. H<sub>2</sub>-TPR

Fig. 11 shows the H<sub>2</sub>-TPR profiles of 3DOM CeO<sub>2</sub>-Co<sub>3</sub>O<sub>4</sub> supports and ~3 wt% Au/CeO<sub>2</sub>-Co<sub>3</sub>O<sub>4</sub> with various Ce/Co molar ratios at 0:1 (pure Co<sub>3</sub>O<sub>4</sub>), 1:5.9, 1:3.2, 1:1.2, 2.5:1, 4.1:1, 4.8:1, 5.9:1, and 1:0 (pure CeO<sub>2</sub>). The H<sub>2</sub>-TPR profile for pure Co<sub>3</sub>O<sub>4</sub> shows two reduction peaks at 325 (α) and 385 (β) °C, which could be attributed to a two-step reduction process of Co<sub>3</sub>O<sub>4</sub> to CoO and CoO to Co, respectively. [45,51,56,57]

The H<sub>2</sub>-TPR profile for pure CeO<sub>2</sub> also exhibits two reduction peaks, and the low-temperature reduction peak located at 530 °C is attributed to the reduction of surface capping oxygen of CeO<sub>2</sub>, while the high-temperature reduction peak at 780 °C is ascribed to the lattice oxygen of CeO<sub>2</sub> [58,59].

For 3DOM CeO<sub>2</sub>-Co<sub>3</sub>O<sub>4</sub> supports, the TPR profiles shows that their reduction peaks initially shift to a low-temperature region and subsequently move to a high-temperature region with the initial increase of Ce/Co molar ratio, attaining the lowest reaction temperature for 3DOM (2.5:1)CeO<sub>2</sub>-Co<sub>3</sub>O<sub>4</sub>, implying the existence of the strongest interaction between CeO<sub>2</sub> and Co<sub>3</sub>O<sub>4</sub> at the molar ratio of 2.5:1. This phenomenon is also found in 3DOM ~3 wt% Au/(2.5:1)CeO<sub>2</sub>-Co<sub>3</sub>O<sub>4</sub> catalyst. The H<sub>2</sub>-TPR profiles indicates that

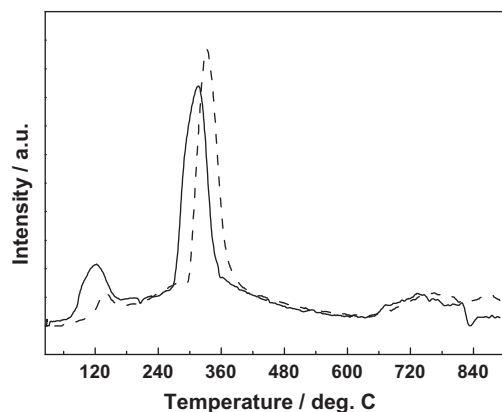


Fig. 12.  $\text{H}_2$ -TPR profiles of the fresh (—) and deactivated (---) 3DOM Au/(2.5:1)  $\text{CeO}_2$ - $\text{Co}_3\text{O}_4$  catalysts.

all reaction peaks of 3DOM  $\text{CeO}_2$ - $\text{Co}_3\text{O}_4$  show a tail, which can be attributed to the reduction of surface oxygen species of  $\text{CeO}_2$  in  $\text{CeO}_2$ - $\text{Co}_3\text{O}_4$  composite support [38].

After loading the Au nanoparticles onto the catalysts, the reducibility of the catalysts is changed due to the interaction of Au nanoparticles with the supports. This causes that the  $\beta$  peak of  $\text{H}_2$ -TPR profiles of 3DOM  $\sim 3$  wt% Au/ $\text{CeO}_2$ - $\text{Co}_3\text{O}_4$  catalysts shifts to lower temperature, leading to the overlapping between  $\alpha$  and  $\beta$  peaks, in comparison with that of their corresponding 3DOM  $\text{CeO}_2$ - $\text{Co}_3\text{O}_4$  supports. However, an additional peak below  $200^\circ\text{C}$  is appeared for 3DOM  $\sim 3$  wt% Au/ $\text{CeO}_2$ - $\text{Co}_3\text{O}_4$  catalysts. As the results were shown in, the actual  $\text{H}_2$  consumption is much higher than the nominal  $\text{H}_2$  consumption of calculated by assuming all present as  $\text{Au}^{3+}$  in all catalysts, suggesting a co-reduction of  $\text{CeO}_2$  and  $\text{Co}_3\text{O}_4$  due to a typical  $\text{H}_2$  spillover effect [44,60]. This means that  $\text{CeO}_2$  and  $\text{Co}_3\text{O}_4$  could be reduced to form a redox couple with ionic Au during HCHO oxidation process, proving that  $\text{CeO}_2$  and  $\text{Co}_3\text{O}_4$  play an important role in catalytic process of HCHO oxidation. The large deviation between the actual and nominal  $\text{H}_2$  consumption implies that there is a strong interaction between Au and  $\text{CeO}_2$ - $\text{Co}_3\text{O}_4$ , which can improve the reducibility of surface oxygen species in  $\text{CeO}_2$  and  $\text{Co}_3\text{O}_4$  [21,61]. The enhanced reduction capability facilitates the oxygen to transfer across the solid-gas interface during the reaction in the catalytic oxidation of HCHO, which may increase the activity of catalytic reaction for 3DOM  $\sim 3$  wt% Au/ $\text{CeO}_2$ - $\text{Co}_3\text{O}_4$  catalysts. Furthermore, all reduction peaks of 3DOM  $\sim 3$  wt% Au/ $\text{CeO}_2$ - $\text{Co}_3\text{O}_4$  catalysts show lower reduction temperature than their corresponding 3DOM  $\text{CeO}_2$ - $\text{Co}_3\text{O}_4$  supports. The reduction peaks shift to lower temperature with the increase of Ce/Co molar ratio. However, a deviation from this order is observed for 3DOM  $\sim 3$  wt% Au/(2.5:1) $\text{CeO}_2$ - $\text{Co}_3\text{O}_4$  catalyst, which may be attributed to the strong interaction in particular between  $\text{CeO}_2$  and  $\text{Co}_3\text{O}_4$  in 3DOM  $\sim 3$  wt% Au/ $\text{CeO}_2$ - $\text{Co}_3\text{O}_4$  catalyst. The introduction of Au in  $\text{CeO}_2$ - $\text{Co}_3\text{O}_4$  supports promotes the reducibility of both  $\text{CeO}_2$  and  $\text{Co}_3\text{O}_4$ , especially for the surface oxygen of  $\text{CeO}_2$ . This may suggest that Au nanoparticles are mainly loaded on  $\text{CeO}_2$  with respect to  $\text{Co}_3\text{O}_4$  [38]. It is well known that high mobility of oxygen in the surface and bulk of the catalyst gives an important contribution to the hydrocarbons oxidation activity [22,62]. So, the catalytic activity is increased by loading Au on 3DOM  $\text{CeO}_2$ - $\text{Co}_3\text{O}_4$  supports due to the activation of oxygen by Au. Fig. 12 comparatively presents the  $\text{H}_2$ -TPR profile of the fresh and deactivated 3DOM  $\sim 3$  wt% Au/(2.5:1) $\text{CeO}_2$ - $\text{Co}_3\text{O}_4$  catalysts. It is obvious that the intensity of a low-temperature reduction peak in the fresh 3DOM  $\sim 3$  wt% Au/(2.5:1) $\text{CeO}_2$ - $\text{Co}_3\text{O}_4$  catalyst is higher. However, the low-temperature reduction peak in the deactivated 3DOM  $\sim 3$  wt% Au/(2.5:1) $\text{CeO}_2$ - $\text{Co}_3\text{O}_4$  catalyst shows a

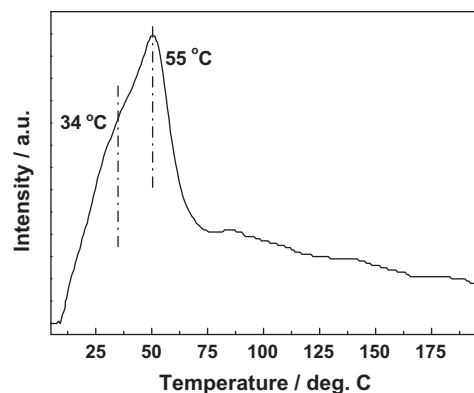


Fig. 13. HCHO-TPSR of 3DOM  $\sim 3$  wt% Au/(2.5:1) $\text{CeO}_2$ - $\text{Co}_3\text{O}_4$  catalysts.

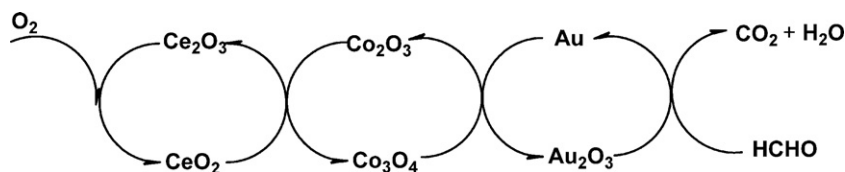
distinct decrease in intensity and shifts to higher temperature. This suggests that the active Au species gradually decreases along with the catalytic reaction continued. In addition, the reducing capacity of the 3DOM  $\sim 3$  wt% Au/(2.5:1) $\text{CeO}_2$ - $\text{Co}_3\text{O}_4$  catalyst also declines, as the reduction peak located in high-temperature region splits into two peaks, and a small reduction peak seated ahead of the original one appears. This indicates that the interaction between the  $\text{CeO}_2$  and  $\text{Co}_3\text{O}_4$  nanoparticles becomes weaker. Furthermore, the high-temperature reduction peak shifts to a higher temperature region compared with the original one, indicating the  $\text{Co}^{3+}$  content decreases in the surface of  $\sim 3$  wt% Au/(2.5:1) $\text{CeO}_2$ - $\text{Co}_3\text{O}_4$  catalysts, implying that the interaction of  $\text{CeO}_2$  and  $\text{Co}_3\text{O}_4$  nanoparticles becomes weaker.

#### 3.4.2. HCHO-TPSR measurement

Fig. 13 shows the HCHO-TPSR measurement of 3DOM  $\sim 3$  wt% Au/(2.5:1) $\text{CeO}_2$ - $\text{Co}_3\text{O}_4$  catalyst. Two reaction peaks located at 34 and  $50^\circ\text{C}$  with a tailing phenomenon are observed. According to the literature [63], the reaction peak in the low-temperature region is due to the formation of  $\text{CO}_2$  through HCHO oxidation, and the  $\text{CO}_2$  generated during the reaction is first absorbed on and then gradually desorbed from the catalyst surface, causing the tailing phenomenon, which is consistent with  $\text{CO}_2$ -TPD tests. The reaction peak in the low-temperature region is split into two peaks moving to a much lower temperature region. This indicates that two Au species of metallic and ionic states exist in the 3DOM Au/ $\text{CeO}_2$ - $\text{Co}_3\text{O}_4$  catalyst, showing the enhanced catalytic activity due to the synergistic effect between  $\text{CeO}_2$  and  $\text{Co}_3\text{O}_4$  supports. Generally, the ionic state Au shows better catalytic activity than metallic state Au, thus the reaction peak observed at  $34^\circ\text{C}$  is ascribed to HCHO oxidation by ionic state Au, while the reaction peak appeared at  $50^\circ\text{C}$  is derived from HCHO oxidation by metallic state Au. The intensity of the reaction peak in the low-temperature region is weaker than that in the high-temperature region suggesting that the content of ionic state Au is less than that of metallic state Au, which is consistent with XPS measurement.

#### 3.4.3. Catalytic mechanism for enhanced HCHO oxidation

3DOM Au/ $\text{CeO}_2$ - $\text{Co}_3\text{O}_4$  catalysts show higher catalytic activity compared to their corresponding 3DOM Au/ $\text{CeO}_2$  and Au/ $\text{Co}_3\text{O}_4$  catalysts. Their catalytic activity is largely correlative to the Ce/Co molar ratio, showing the optimum catalytic activity with Ce/Co molar ratio at 2.5:1 due to the strong synergistic effect between  $\text{CeO}_2$  and  $\text{Co}_3\text{O}_4$  supports. The catalytic mechanism of HCHO oxidation over 3DOM Au/ $\text{CeO}_2$ - $\text{Co}_3\text{O}_4$  catalysts follows the one previously reported for 3DOM Au/ $\text{CeO}_2$ - $\text{Co}_3\text{O}_4$  catalysts [55]. The enhancement of catalytic activity for HCHO oxidation over 3DOM



**Scheme 1.** Schematic illustration of catalytic mechanism for enhanced catalytic oxidation of HCHO over 3DOM Au/CeO<sub>2</sub>-Co<sub>3</sub>O<sub>4</sub> catalysts.

Au/CeO<sub>2</sub>-Co<sub>3</sub>O<sub>4</sub> catalysts might be due to the fact that the incorporation of Co<sub>3</sub>O<sub>4</sub> into the CeO<sub>2</sub> support generates a synergistic effect between the CeO<sub>2</sub> and Co<sub>3</sub>O<sub>4</sub> supports, speeding up the active oxygen migration rate and enhancing the mobility of oxygen on the catalyst surface, thus resulting in improved catalytic activity. The synergistic effect between CeO<sub>2</sub> and Co<sub>3</sub>O<sub>4</sub> supports for enhancing the catalytic activity of 3DOM Au/CeO<sub>2</sub>-Co<sub>3</sub>O<sub>4</sub> catalyst is schematically illustrated in Scheme 1. From Scheme 1, it can be seen that when the synergistic effect exists between the CeO<sub>2</sub> and Co<sub>3</sub>O<sub>4</sub> supports, the Co<sub>3</sub>O<sub>4</sub> may participate in oxygen transfer during the HCHO catalytic oxidation process. The Ce<sub>2</sub>O<sub>3</sub> may initially interact with oxygen and change into CeO<sub>2</sub>. Then, with the assistance of Co<sub>3</sub>O<sub>4</sub>, the oxygen is continuously transferred to Co<sub>3</sub>O<sub>4</sub> from CeO<sub>2</sub>, and then is further transferred to Au, making Au change into the oxidation state. Through this process, the oxygen is activated and transferred to HCHO from Au<sub>2</sub>O<sub>3</sub>, making HCHO oxidation happen. Due to the existence of the synergistic effect between CeO<sub>2</sub> and Co<sub>3</sub>O<sub>4</sub>, the oxygen migration rate is accelerated, and more active oxygen interacts with the reactant of HCHO, thus greatly improving the catalytic activity of the 3DOM Au/CeO<sub>2</sub>-Co<sub>3</sub>O<sub>4</sub> catalyst, resulting in high catalytic activity in relatively low temperature. However, to maximize the synergistic effect between CeO<sub>2</sub> and Co<sub>3</sub>O<sub>4</sub>, the optimum Ce/Co molar ratio is required (2.5:1 in this study). When the Ce/Co molar ratio is highly deviated from this number, the phase separation of CeO<sub>2</sub> and Co<sub>3</sub>O<sub>4</sub> may occur and the surface composition of 3DOM Au/CeO<sub>2</sub>-Co<sub>3</sub>O<sub>4</sub> catalyst may be changed. Therefore, the synergistic effect may be weakened, decreasing the catalytic activity of the 3DOM Au/CeO<sub>2</sub>-Co<sub>3</sub>O<sub>4</sub> catalyst.

## Conclusions

A precursor thermal decomposition-assisted colloidal crystal templating method was developed for creating 3DOM Au/CeO<sub>2</sub>-Co<sub>3</sub>O<sub>4</sub> catalysts. The obtained Au/CeO<sub>2</sub>-Co<sub>3</sub>O<sub>4</sub> catalysts had well-defined 3DOM structures with adjustable pore sizes, and nanoporous walls resulted from the thermal decomposition of Co and Ce oxalate precursors during the preparation. The compositions, phase structures, porous architectures, and surface elemental compositions and valence states of 3DOM Au/CeO<sub>2</sub>-Co<sub>3</sub>O<sub>4</sub> catalysts were found to have significant effects on their catalytic activity for HCHO oxidation. The 3DOM ~3 wt% Au/(2.5:1)CeO<sub>2</sub>-Co<sub>3</sub>O<sub>4</sub> catalyst exhibits the superior catalytic activity for HCHO oxidation with 100% conversion rate at the relatively low temperature of ~39 °C. The catalytic mechanism of the synergistic effect between CeO<sub>2</sub> and Co<sub>3</sub>O<sub>4</sub> supports, which largely accelerates the surface active oxygen migration and activates the Au species, was proposed to explain the enhanced HCHO catalytic oxidation over 3DOM Au/CeO<sub>2</sub>-Co<sub>3</sub>O<sub>4</sub> catalysts. The well-controlled method for creation of macroporous and mesoporous structured 3DOM Au/CeO<sub>2</sub>-Co<sub>3</sub>O<sub>4</sub> catalysts may be available for generation of other catalytic materials with mixed macroporous and mesoporous structures. The superior catalytic activity of 3DOM Au/CeO<sub>2</sub>-Co<sub>3</sub>O<sub>4</sub> catalysts makes them potentially applicable to indoor formaldehyde decontamination and industrial catalysis.

## Acknowledgments

We gratefully acknowledge the financial support from National High Technology Research and Development Program (863 program, 2010AA03A407), National Natural Science Foundation of China (20961005), Key project of Inner Mongolia National Natural Science Foundation (2010ZD03), and Program for New Century Excellent Talents in University (NCET-10-0907), the Science and Technology Innovation Team of Inner Mongolia University on Research of Micron and Nanometer Magnetic Functional Material (Grant No. 10013-12110605).

## Appendix A. Supplementary data

Supplementary data associated with this article can be found in the online version, at <http://dx.doi.org/10.1016/j.apcatb.2012.08.005>.

## References

- [1] Y. Shi, Y. Wan, D. Zhao, *Chemical Society Reviews* 40 (2011) 3854.
- [2] A. Navrotsky, O. Trofymuk, A.A. Levchenko, *Chemical Reviews* 109 (2009) 3885.
- [3] L. Lu, A. Eychmüller, *Accounts of Chemical Research* 41 (2008) 244.
- [4] C. Li, B. Liu, Y. Jin, J. Zhang, *Catalysis: Principles, Types and Applications*, Nova Science Publishers, Inc., New York, 2012, pp. 1–29.
- [5] F. Marlow, Muldarisnur, P. Sharifi, R. Brinkmann, C. Mendive, *Angewandte Chemie International Edition* 48 (2009) 6212.
- [6] K.T. Lee, J.C. Lytle, N.S. Ergang, S.M. Oh, A. Stein, *Advanced Functional Materials* 15 (2005) 547.
- [7] J.S. Sakamoto, B. Dunn, *Journal of Materials Chemistry* 12 (2002) 2859.
- [8] X. Wang, L. Yuan, J. Qu, Y. Zhang, X. Zhang, *Acta Chimica Sinica* 68 (2010) 2238.
- [9] J. Zhang, Y. Jin, C. Li, Y. Shen, L. Han, Z. Hu, X. Di, Z. Liu, *Applied Catalysis B* 91 (2009) 11.
- [10] C. Li, Y. Shen, M. Jia, S. Sheng, M.O. Adebajo, H. Zhu, *Catalysis Communications* 9 (2008) 355.
- [11] Y. Shen, X. Yang, Y. Wang, Y. Zhang, H. Zhu, L. Gao, M. Jia, *Applied Catalysis B* 79 (2008) 142.
- [12] H.F. Li, N. Zhang, P. Chen, M.F. Luo, J.Q. Lu, *Applied Catalysis B* 110 (2011) 279.
- [13] C. Ma, D. Wang, W. Xue, B. Dou, H. Wang, Z. Hao, *Environmental Science & Technology* 45 (2011) 3628.
- [14] X. Tang, J. Chen, Y. Li, Y. Li, Y. Xu, W. Shen, *Chemical Engineering Journal* 118 (2006) 119.
- [15] X. Tang, J. Chen, X. Huang, Y. Xu, W. Shen, *Applied Catalysis B* 81 (2008) 115.
- [16] H. Huang, D.Y.C. Leung, *ACS Catalysis* 1 (2011) 348.
- [17] S.J. Park, I. Bae, I.-S. Nama, B.K. Cho, S.M. Jung, J.-H. Lee, *Chemical Engineering Journal* 195–196 (2012) 392.
- [18] S.S. Kim, K.H. Park, S.C. Hong, *Applied Catalysis A: General* 398 (2011) 96.
- [19] H. Huang, D.Y.C. Leung, *Journal of Catalysis* 280 (2011) 60.
- [20] L. Wang, M. Sakurai, H. Kameyama, *Journal of Hazardous Materials* 167 (2009) 399.
- [21] N. An, Q. Yu, G. Liu, S. Li, M. Jia, W. Zhang, *Journal of Hazardous Materials* 186 (2011) 1392.
- [22] Y. Zhang, Y. Shen, X. Yang, S. Sheng, T. Wang, M.F. Adebajo, H. Zhu, *Journal of Molecular Catalysis A: Chemical* 316 (2010) 100.
- [23] Y.C. Hong, K.Q. Sun, K.H. Han, G. Liu, B.Q. Xu, *Catalysis Today* 158 (2010) 415.
- [24] V.A. de la Peña O'Shea, M.C. Álvarez-Galván, J.L.G. Fierro, P.L. Arias, *Applied Catalysis B* 57 (2005) 191.
- [25] J. Huang, L.C. Wang, Y.M. Liu, Y. Cao, H.Y. He, K.N. Fan, *Applied Catalysis B* 101 (2011) 560.
- [26] A. Sandoval, A. Aguilar, C. Louis, A. Traverse, R. Zanella, *Journal of Catalysis* 281 (2011) 40.
- [27] Z. Hou, N. Theysen, A. Brinkmann, K.V. Klementiev, W. Gruenert, M. Buehl, W. Schmidt, B. Spliethoff, B. Tesche, C. Weidenthaler, W. Leitner, *Journal of Catalysis* 258 (2008) 315.
- [28] K. Yamaguchi, J.W. Kim, J. He, N. Mizuno, *Journal of Catalysis* 268 (2009) 343.
- [29] C.M.A. Parlett, D.W. Bruce, N.S. Hondow, A.F. Lee, K. Wilson, *ACS Catalysis* 1 (2011) 636.



- [30] A. Molnar, *Chemical Reviews* 111 (2011) 2251.
- [31] A. Balanta, C. Godard, C. Claver, *Chemical Society Reviews* 40 (2011) 4973.
- [32] Q.Z. Wu, Y. Shen, J.F. Liao, Y.G. Li, *Materials Letters* 58 (2004) 2688.
- [33] H.W. Yan, C.F. Blanford, B.T. Holland, W.H. Smyrl, A. Stein, *Chemistry of Materials* 12 (2000) 1134.
- [34] D.Y. Wang, R.A. Caruso, F. Caruso, *Chemistry of Materials* 13 (2001) 364.
- [35] Y.G. Zhang, Z.B. Lei, J.M. Li, S.M. Lu, *New Journal of Chemistry* 25 (2001) 1118.
- [36] C.Y. Ma, Z. Mu, J.J. Li, Y.G. Jin, J. Cheng, G.Q. Lu, Z.P. Hao, S.Z. Qiao, *Journal of American Chemical Society* 132 (2010) 2608.
- [37] X. Xie, Y. Li, Z.-Q. Liu, M. Haruta, W. Shen, *Nature* 458 (2009) 746.
- [38] H. Wang, H. Zhu, Z. Qin, G. Wang, F. Liang, J. Wang, *Catalysis Communications* 9 (2008) 1487.
- [39] Q. Guo, Y. Liu, *Applied Catalysis B* 82 (2008) 19.
- [40] M. Kang, M.W. Song, C.H. Lee, *Applied Catalysis A* 251 (2003) 143.
- [41] J.Y. Luo, M. Meng, X. Li, X.G. Li, Y.Q. Zha, T.D. Hu, Y.N. Xie, J. Zhang, *Journal of Catalysis* 254 (2008) 310.
- [42] L.F. Liotta, G. Di Carlo, G. Pantaleo, A.M. Venezia, G. Deganello, *Topics in Catalysis* 52 (2009) 1989.
- [43] H. Wang, H. Zhu, Z. Qin, F. Liang, G. Wang, J. Wang, *Journal of Catalysis* 264 (2009) 154.
- [44] A.M. Venezia, G. Pantaleo, A. Longo, G. Di Carlo, M.P. Casaletto, F.L. Liotta, G. Deganello, *The Journal of Physical Chemistry B* 109 (2005) 2821.
- [45] L.F. Liotta, G. Di Carlo, A. Longo, G. Pantaleo, A.M. Venezia, *Catalysis Today* 139 (2008) 174.
- [46] Q. Fu, H. Saltsburg, M. Flytzani-Stephanopoulos, *Science* 301 (2003) 935.
- [47] D.A. Bulushev, I. Yuranov, E.I. Suvorova, P.A. Buffat, L. Kiwi-Minsker, *Journal of Catalysis* 224 (2004) 8.
- [48] L. Fan, N. Ichikuni, S. Shimazu, T. Uematsu, *Applied Catalysis A* 246 (2003) 87.
- [49] W. Deng, J. Jesus, H. Saltsburg, M. Flytzanistephanopoulos, *Applied Catalysis A* 291 (2005) 126.
- [50] M. Manzoli, F. Boccuzzi, A. Chiorino, F. Vindigni, W.L. Deng, M. Flytzani-Stephanopoulos, *Journal of Catalysis* 245 (2007) 308.
- [51] L. Liotta, G. Dicarolo, G. Pantaleo, A. Venezia, G. Deganello, *Applied Catalysis B* 66 (2006) 217.
- [52] H. Cordatos, T. Bunluesin, J. Stubenrauch, J.M. Vohs, R.J. Gorte, *Journal of Physical Chemistry* 100 (1996) 785.
- [53] M. Hoang, A.E. Hughes, T.W. Turney, *Applied Surface Science* 72 (1993) 55.
- [54] Y.I.K. Ichimura, I. Yasumori, *Bulletin of the Chemical Society of Japan* 53 (1980) 3044.
- [55] H. Wang, J. Ye, Y. Liu, Y. Li, Y. Qin, *Catalysis Today* 129 (2007) 305.
- [56] G. Jacobs, T.K. Das, Y.Q. Zhang, J.L. Li, G. Racollet, B.H. Davis, *Applied Catalysis A* 233 (2002) 263.
- [57] D. Terribile, A. Trovarelli, C. de Leitenburg, A. Primavera, G. Dolcetti, *Catalysis Today* 47 (1999) 133.
- [58] J. Kaspar, P. Fornasiero, M. Graziani, *Catalysis Today* 50 (1999) 285.
- [59] G.I. Golodets, *Heterogeneous Catalytic Reactions Involving Molecular Oxygen*, Elsevier, Amsterdam, 1983, pp. 437.
- [60] O.H. Laguna, F.R. Sarria, M.A. Centeno, J.A. Odriozola, *Journal of Catalysis* 276 (2010) 360.
- [61] Y. Xia, H. Dai, L. Zhang, J. Deng, H. He, C.T. Au, *Applied Catalysis B: Environmental* 100 (2010) 229.
- [62] S. Imamura, D. Uchiho, K. Utani, T. Ito, *Catalysis Letters* 24 (1994) 377.
- [63] B. Liu, C. Li, Y. Zhang, Y. Liu, W. Hu, Q. Wang, L. Han, J. Zhang, *Applied Catalysis B: Environmental* 111–112 (2012) 467.